Journal of Nanobiotechnology

RESEARCH

Open Access

Black phosphorus nanosheet-enabled ROS-adaptive core-shell microneedles orchestrate immunoredox remodeling and neurotrophic regeneration for facial nerve repair

Qiang Zhou[1†], Qingyue Yuan[2†], Peng Lai[3†], Shuo Li[1†], Xianlong Wang[1,4], Yuqi Han[1], Shuyi Lin[1], Chenhao Fang[1], Kaizheng Qu[5], Ziwei Zhang[1], Ying Ran[6], Yiheng Yang[1,4*], Yavuz Nuri Ertas[7,8*], Liangle Liu[9*] and Xianzhen Chen[1,2*]

Abstract

Background Facial nerve injury often results in persistent facial paralysis because the early oxidative and inflammatory microenvironment compromises subsequent neurotrophic repair. Existing therapies are limited by insufficient spatiotemporal control over antioxidative and neurotrophic interventions at the lesion site, leading to suboptimal regenerative outcomes. Black phosphorus nanosheets (BPNs) have emerged as promising nanotherapeutics owing to their strong ROS-scavenging capacity, immunomodulatory potential, and favorable biodegradability. However, strategies that integrate BPN-mediated microenvironment regulation with sustained neurotrophic stimulation for facial nerve repair remain largely unexplored. Here, we developed a ROS-adaptive core–shell microneedle nanoplatform that sequentially remodels the oxidative–inflammatory niche and subsequently promotes neurotrophic regeneration through staged delivery of BPNs and nerve growth factor (NGF).

Results The microneedle shell consisted of a dynamic hyaluronic acid–phenylboronic acid/poly(vinyl alcohol) network loaded with BPNs, while the GelMA hydrogel core served as a reservoir for sustained NGF release. Under ROS conditions, cleavage of boronate ester bonds accelerated shell degradation and promoted BPN release. The released nanosheets reduced intracellular ROS, were associated with NRF2/HO-1 antioxidant pathway activation and NF-κB inflammatory signaling suppression in macrophages, and promoted polarization toward a pro-regenerative M2-like phenotype. This immunoredox modulation reduced oxidative stress and inflammatory mediator expression

†Qiang Zhou, Qingyue Yuan, Peng Lai and Shuo Li contributed equally to this work.

*Correspondence:
Yiheng Yang
yangyiheng@tongji.edu.cn
Yavuz Nuri Ertas
yavuznuri@gmail.com
Liangle Liu
liuliangle@wmu.edu.cn
Xianzhen Chen
chenxianzheny@126.com

Full list of author information is available at the end of the article

while establishing a more permissive microenvironment for neural repair. Subsequently, controlled NGF release from the core enhanced TrkA/AKT/ERK signaling, promoting neuronal differentiation, neurite extension, and axonal regeneration. The platform also improved Schwann cell proliferation, migration, and neurotrophic secretion, supporting remyelination and axonal guidance. In a mouse facial nerve crush model, treatment with BPN/NGF core-shell microneedles reduced oxidative damage and inflammatory infiltration, improved myelin sheath integrity and nerve ultrastructure, and accelerated early functional recovery compared with blank or single-cargo microneedle treatments.

Conclusion This study presents a BPN-enabled ROS-responsive microneedle nanoplatform that addresses stage-specific barriers in facial nerve repair by sequentially regulating immunoredox responses and stimulating neurotrophic signaling. These findings highlight a promising nanobiotechnology strategy for peripheral nerve regeneration and may provide a broadly applicable framework for ROS-associated tissue injuries.

Keywords Black phosphorus nanosheets, ROS-responsive delivery, Microneedle, Facial nerve regeneration, Immunoredox modulation, Macrophage polarization, Nerve growth factor (NGF), Peripheral nerve repair, Spatiotemporal drug delivery

Graphical Abstract

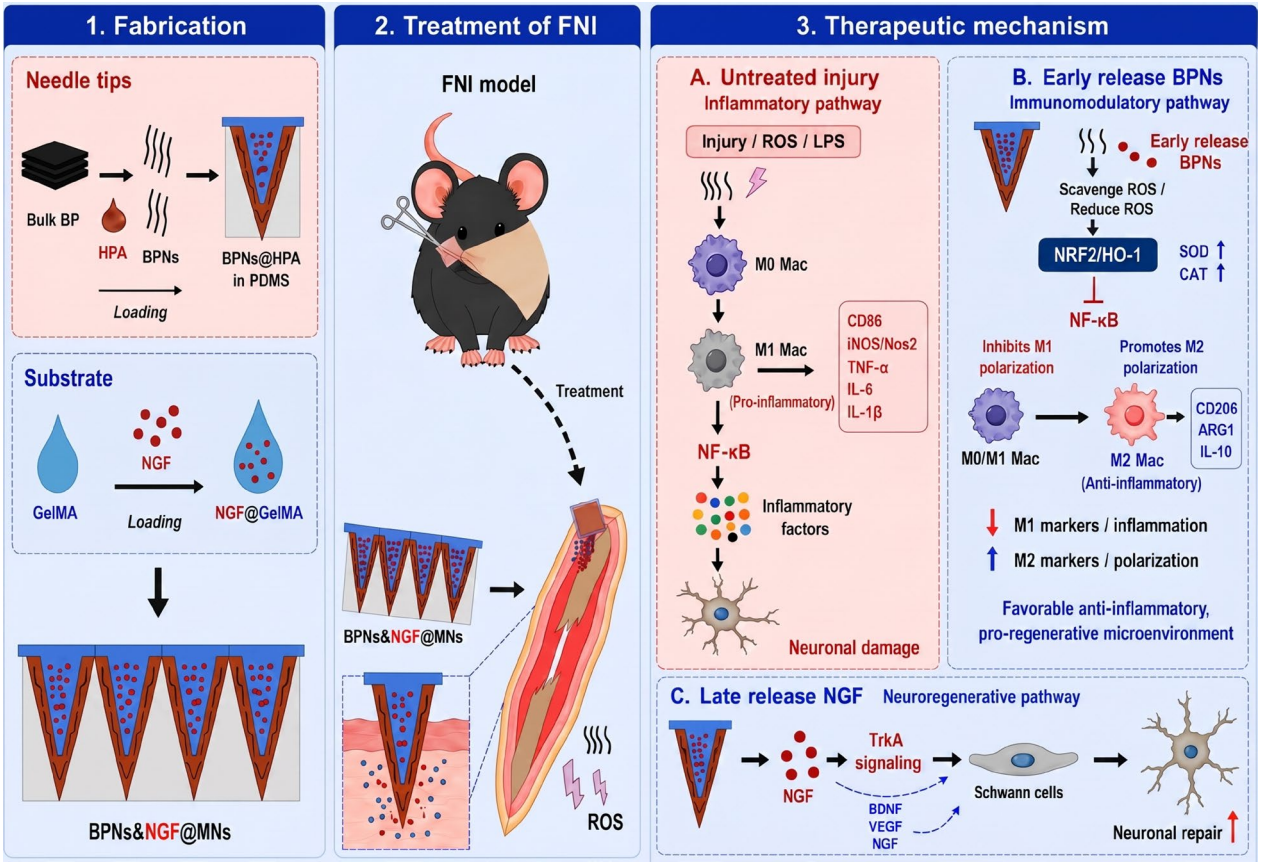

Introduction

Facial nerve injury (FNI) is a common type of peripheral nerve injury, typically caused by trauma, surgery, or viral infections, resulting in functional deficits such as facial paralysis, impaired eyelid closure, and abnormalities in facial expression [1]. This injury significantly impacts the patient's daily life, psychological well-being, and social interactions, and may result in long-term functional impairment [2]. Following FNI, Wallerian degeneration (WD) occurs, characterized by rapid axonal degeneration and myelin clearance [1]. During the repair process, Schwann cells and macrophages play crucial roles. Schwann cells assist in nerve axon recovery and function restoration through demyelination and remyelination, while macrophages clear necrotic tissue at the injury site and release repair-promoting factors

to aid nerve regeneration [3]. However, oxidative stress injury remains a significant barrier to facial nerve repair. After nerve injury, increased oxidative stress exacerbates cellular damage and functional impairment [4]. Oxidative stress is caused by the excessive production of free radicals and reactive oxygen species (ROS), which damage cell membranes, proteins, and DNA, thereby further impairing nerve tissue [5]. Although the initial inflammatory response is beneficial for clearing debris and releasing growth factors, excessive or chronic inflammation can inhibit nerve regeneration. Therefore, an effective FNI therapy must rapidly resolve the early oxidative–inflammatory barrier while preserving a permissive niche for subsequent neurotrophic regeneration, which remains challenging using conventional bolus injections or single-factor delivery.

Nerve growth factor (NGF), a crucial neurotrophic factor, is widely utilized in the repair of nerve injuries, including FNI [6]. NGF ligation to its high-affinity receptor, TrkA, triggers a cascade of intracellular signaling pathways, most notably the PI3K/AKT, MAPK/ERK, and CREB axes, which collectively govern the survival, differentiation, and regenerative repair of neural cells [7, 8]. However, the clinical use of NGF faces limitations, especially in early oxidative stress environments, where its efficacy is markedly suppressed [9]. Following nerve injury, oxidative stress and excessive ROS accumulation damage neural tissue, reducing the bioactivity of neurotrophic factors. Specifically, ROS not only degrades NGF itself but may also disrupt its binding to target cells and signal transmission by altering the structure or function of NGF receptors [10, 11]. Furthermore, the oxidative stress environment accelerates NGF degradation, making it difficult to maintain sufficient activity and effective concentrations during treatment. Consequently, when NGF is used alone to treat FNI, its efficacy is often limited under oxidative stress, failing to achieve sustained and precise therapeutic effects. To overcome the limitations of NGF therapy in oxidative stress environments, black phosphorus nanosheets (BPNs), as a novel antioxidant material, demonstrate significant potential for combined use with NGF. BPNs, as two-dimensional materials, have become a substantial focus in neurotrauma research due to their exceptional antioxidant properties and excellent biocompatibility [12–14]. They mitigate oxidative stress-induced damage to neural tissue by scavenging excess ROS, which helps suppress unnecessary inflammatory responses. Additionally, BPNs not only modulate immune cell activity, facilitating the transition of macrophages from the pro-inflammatory M1 to the anti-inflammatory M2 phenotype, but also promote the proliferation and differentiation of Schwann cells and neurons, thereby accelerating nerve repair [13, 15]. Moreover, the oxidative metabolism of BPNs generates phosphate products that create a "phosphorus-rich" environment, supporting myelin regeneration and guiding axonal growth [12]. Collectively, FNI repair requires a delivery strategy that (i) responds to the pathological ROS burst to rapidly suppress oxidative–inflammatory damage and (ii) subsequently provides sustained neurotrophic cues for regeneration. Such spatiotemporally programmed delivery remains underdeveloped for facial nerve repair.

However, despite the promising antioxidant and anti-inflammatory effects of BPNs combined with NGF for repairing FNI, their application is limited by rapid drug metabolism and challenges in effectively delivering these therapies to the injury site [16, 17]. Stimuli-responsive microneedle systems, including polymeric and dynamically crosslinked platforms, have been widely explored for on-demand drug delivery and provide an important conceptual basis for microneedle system design and the ROS-responsive release mechanism used in this study [18–21]. To address this issue, we propose employing a dual-layer core-shell microneedle system (BPNs&NGF@MNs, abbreviated as BNMNs), in which the outer layer is loaded with BPNs and the inner layer with NGF, thereby achieving sequential antioxidant and regenerative therapy (Scheme 1A). In the bilayer microneedle design, the outer shell is composed of 3-aminophenylboronic acid (HA-PBA) grafted to hyaluronic acid and crosslinked with polyvinyl alcohol (PVA). The boronate ester bonds are responsive to ROS and can release BPNs under ROS stimulation, exerting anti-inflammatory effects. The core, composed of GelMA hydrogel, enables sustained NGF release (Scheme 1B). In vivo, BNMNs demonstrated a dual-phase therapeutic effect in the context of FNI. During the early phase of the injury, BNMNs efficiently released BPNs in response to the oxidative stress microenvironment of the FNI site. These BPNs exhibited potent antioxidant and anti-inflammatory properties, effectively mitigating the oxidative damage and inflammation associated with nerve injury. As the treatment progressed, BNMNs released NGF, which played a crucial role in promoting neuronal repair and regeneration. Meanwhile, in vitro, BNMNs exhibited strong antioxidant and anti-inflammatory effects by suppressing ROS induced by LPS, reducing oxidative stress, and inhibiting macrophage polarization toward the pro-inflammatory M1 phenotype, while promoting polarization towards the anti-inflammatory M2 phenotype. RNA sequencing revealed that BNMNs inhibited the NF-κB pathway and activated the NRF2/HO-1 antioxidant pathway, enhancing macrophage antioxidant capacity and facilitating M2 polarization. Additionally, BPNs release phosphate ions upon complete oxidation, which, together with the subsequent release of NGF, promotes neuronal differentiation and enhances Schwann cell proliferation, migration,

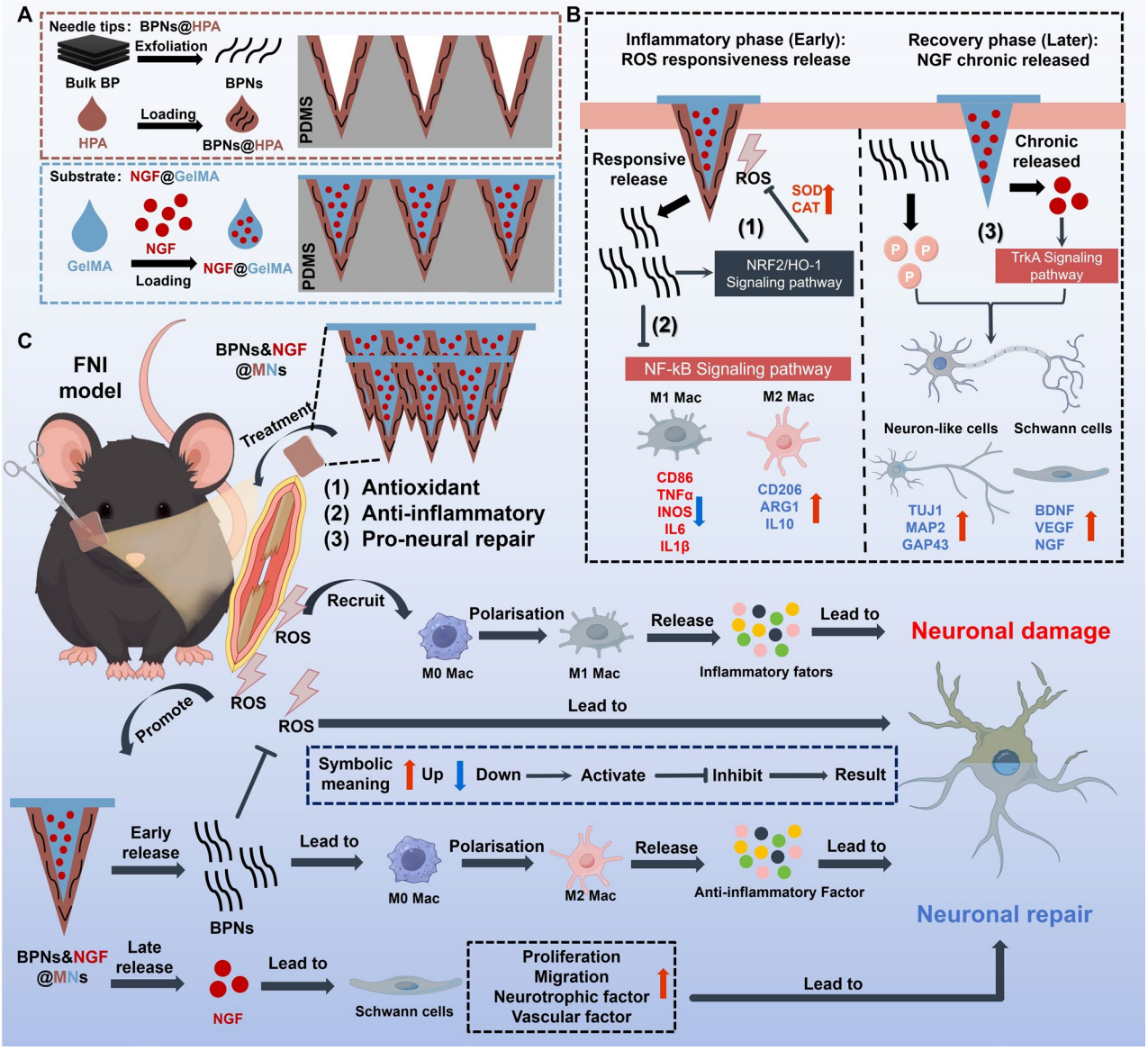

Scheme 1 Schematic of a programmable black phosphorus nanosheets (BPNs)/nerve growth factor (NGF)-loaded core–shell microneedles (BPNs&NGF@MNs, abbreviated as BNMNs) enabling a temporally staged transition from antioxidative/anti-inflammatory to pro-regenerative intervention in a mouse facial nerve injury (FNI) model. (**A**) BPNs-loaded HA-PBA/PVA form the shell at the needle tips, while NGF@GelMA constitutes the core on the substrate; vacuum casting, crosslinking, and drying yield a core–shell array. (**B**) This design enables time-controlled release. During the early inflammatory phase, ROS-responsive BPNs are initially released to (1) scavenge reactive oxygen species, activate the NRF2/HO-1 pathway, and (2) suppress NF-κB signaling. This promotes the shift of macrophages from the pro-inflammatory M1 phenotype to anti-inflammatory M2 phenotype (CD86, TNF-α, iNOS, IL-6, IL-1β decrease; CD206, ARG1, IL-10 increases). During the later recovery phase, continuously released NGF (3) activates the TrkA pathway in neuron-like cells (PC12 cells), promoting increased expression of TUJ1, MAP2, and GAP43. Additionally, it stimulates Schwann cells (RSC96 cells) to release BDNF, NGF, and VEGF. (**C**) In the FNI model, the BNMNs are designed to deliver both antioxidant and anti-inflammatory interventions in the early stage, followed by pro-regenerative treatment in the recovery phase. The initial release of BPNs targets the ROS response, promoting macrophage polarization towards the anti-inflammatory M2 phenotype, decreasing pro-inflammatory cytokines, and enhancing the expression of anti-inflammatory cytokines, which accelerates tissue repair by modulating the immune environment. The late, sustained release of NGF promotes neuronal differentiation, axonal regeneration, and myelin regeneration. This dual-phase treatment promotes both inflammatory resolution and subsequent neural repair, improving the functional recovery of the facial nerve after injury

and vascular network formation, thereby supporting nerve regeneration and functional recovery (Scheme 1C). Therefore, this bilayer core-shell microneedle system not only improves the precision of drug delivery but also enhances therapeutic efficacy by controlling time-sensitive drug release, providing a promising approach for repairing FNI.

Experimental section

Materials and reagents

Black phosphorus (BP) powder and NGF were purchased from Zhongke Experimental Materials (Henan, China). Hyaluronic acid (HA), 1-ethyl-3-(3-dimethylaminopropyl) carbodiimide hydrochloride (EDC), N-hydroxysuccinimide (NHS), N-methylpyrrolidone (NMP), 3-(3,4-dihydroxyphenyl) propionic acid, 3-aminophenylboronic acid (PBA), methacrylic anhydride, polyvinyl alcohol (PVA), and lithium acyl phosphate were obtained from Aladdin (Shanghai, China). Enzyme-linked immunosorbent assay (ELISA) kits, including IL-1β (Cat# ZC-37974), TNF-α (Cat# ZC-37974), NGF (Cat# ZC-38640), BDNF (Cat# ZC-38512), and VEGF (Cat# ZC-38844), were purchased from Shanghai Zhuocai Biotechnology Co., Ltd. (Shanghai, China). Cell Counting Kit-8 (CCK8; Cat# C0037), Calcein/PI cell viability and cytotoxicity assay kits (Cat# C2015), ROS assay kits (Cat# S0033S), Hoechst 33,342 (Cat# C1022), DAPI (Cat# C1002), Malachite Green Phosphate Detection Kit (Cat# S0196), and qPCR Primer Pairs (Mouse Tnf qPCR Primer Pair-QM05522S, Mouse Il6 qPCR Primer Pair QM03482S, Mouse Nos2 qPCR Primer Pair-QM04186S, Mouse Il1b qPCR Primer Pair-QM03422S, Mouse Arg1 qPCR Primer Pair-QM09790S, Mouse Gap43 qPCR Primer Pair-QM13570S, Mouse Tubb3 qPCR Primer Pair-QM05682S, Mouse Map2 qPCR Primer Pair-QM04006S, Mouse Actb qPCR Primer Pair-QM00002S), were obtained from Beyotime (Shanghai, China). Hydrogen peroxide (H_2O_2) assay kits, superoxide dismutase (SOD) assay kits, and catalase (CAT) assay kits were purchased from Solarbio (Beijing, China). Primary antibodies for western blotting, including NRF2 (1: 1000; Cat# HA723302), phospho-NRF2 (p-NRF2; 1: 2000; Cat# ET1608-28), HO1 (1: 1000; Cat# HA721854), CREB (1: 500; Cat# ET1601-15), p-CREB (1: 500; Cat# ET7107-93), AKT (1: 2000; Cat# ET1609-51), p-AKT (1: 5000; Cat# ET1607-73), β-actin (1:10000; Cat# HA722023) and Goat Anti-Rabbit IgG HRP (1: 10000; Cat# HA1001) were purchased from Huaan Biotechnology Co., Ltd. (Hangzhou, China). Primary antibodies targeting P65 (1: 1000; Cat# 8242), p-P65 (1: 1000; Cat# 3033), IKBα (1: 1000; Cat# 4812), p-IKBα (1: 1000; Cat# 2859), ERK (1: 1000; Cat# 4695) and p-ERK (1: 1000; Cat# 4370) were purchased from Cell Signaling Technology (Boston, USA). Antibodies for immunofluorescence, including ARG1 (1:400; Cat# DF6657) and iNOS (1:400; Cat# AF0199), Goat Anti-Rabbit IgG (H + L) FITC-conjugated (1:500; Cat# S0008), and Goat Anti-Rabbit IgG (H + L) CY3-conjugated (1:500; Cat# S0011) were purchased from Affinity Biopharmaceutical Co., Ltd. (Melbourne, Australia). Nuclear protein and plasma protein extraction kit (Cat# PH0324) was purchased from Phygene (Fujian, China). Lipopolysaccharide (LPS) was obtained from Sigma (MO, USA). FITC-labeled anti-mouse CD86 antibody was purchased from Elabscience (Wuhan, China), and FITC-labeled anti-mouse CD206 antibody was purchased from BioLegend (Beijing, China). EdU assay kits were obtained from Sunncell Biotechnology Co., Ltd. Phosphate-buffered saline (PBS, pH = 7.4) and cell culture-associated medium were obtained from Gibco (California, USA) and Servicebio (Wuhan, China). All materials were used as received. All solutions were freshly prepared prior to each experiment for immediate use.

Cell culture

Cell lines, including RAW264.7, PC12, RSC96, and HUVEC cells, were obtained from Shanghai Chenying Biotechnology Co., Ltd. (Shanghai, China). RAW264.7, RSC96, and HUVEC cells were maintained in Dulbecco's Modified Eagle Medium (DMEM, high glucose; Gibco, USA) supplemented with 10% fetal bovine serum (FBS; Gibco, USA) and 1% penicillin/streptomycin (P/S; Gibco, USA) at 37 °C in a humidified incubator containing 5% CO_2. PC12 cells were cultured in RPMI-1640 medium (Gibco, USA) supplemented with 10% FBS and 1% P/S under the same incubation conditions. Culture media were replaced every 1–2 days, and cells were subcultured when they reached ~ 70–80% confluence.

Preparation and characterization of BPNs

Using BP powder as the primary raw material, BPNs were prepared via liquid-phase exfoliation [22]. The specific steps are as follows: A total of 10 mg of bulk BP powder was finely ground into powder using an agate mortar and subsequently dispersed in 25 mL of NMP. The suspension was sonicated for 30 min to achieve maximum dispersion, followed by ultrasonic cell disruption (Xiaomei Ultrasound Instruments Kunshan Co., Ltd., China) at a power of 650 W for 48 h to induce liquid-phase exfoliation. After exfoliation, the resulting dispersion was subjected to gradient centrifugation. Initially, the dispersion was centrifuged at 5000 rpm for 10 min to remove the unexfoliated thick black phosphorus crystals from the bottom. The supernatant was then centrifuged at 8000 rpm for 10 min to separate relatively thicker black phosphorus flakes. The supernatant was then centrifuged at 12,000 rpm for 1 h, and the collected precipitate was designated as the desired BPNs. The BPNs were purified through three washing cycles with anhydrous ethanol,

followed by three additional cycles with deionized water to ensure complete removal of residual solvents. The final product was resuspended and stored in a sealed container at 4 °C for further use.

To comprehensively characterize the physicochemical properties of the obtained BPNs, a series of structural, morphological, and compositional analyses was performed. The morphology of BPNs was observed by transmission electron microscopy (TEM; Tecnai G2 F20, FEI, USA) using carbon-supported copper grids, and elemental mapping was conducted by energy-dispersive X-ray spectroscopy (EDS). Scanning electron microscopy (SEM; JSM-6700 F, JEOL, Japan) was employed to analyze surface morphology. Atomic force microscopy (AFM; Dimension Icon, Bruker, Germany) was used to determine the thickness and surface roughness of BPNs. Dynamic light scattering (DLS) and zeta potential analyses were performed using a Malvern Zetasizer Nano ZS (Malvern Panalytical, UK) to determine hydrodynamic size distribution and colloidal stability. Fourier-transform infrared spectroscopy (FTIR; Tensor 27, Bruker, Germany) was employed to evaluate chemical bonding and optical properties. Raman spectroscopy (LabRAM, Horiba, Japan) was conducted to confirm the characteristic peaks of BPNs. The elemental composition and surface chemical states of BPNs were analyzed by X-ray photoelectron spectroscopy (XPS; Nexsa X, Thermo Fisher Scientific, USA).

In vitro cytotoxicity assay of BPNs and NGF

RAW264.7 cells (5×10^3) were seeded in a 96-well plate and cultured for 12 h. To determine the cytotoxicity of BPNs, RAW264.7 cells were treated with 1, 3, 5, 10, 20, 30, 40, 50, 75, or 100 μg/mL BPNs for 1 day. To determine NGF cytotoxicity, RAW264.7 cells were treated with 5, 10, 25, 50, 75, 100, 150, 175, or 200 ng/mL NGF for 24 h. RAW264.7 cells were then incubated with the CCK-8 assay solution for 30 min, and absorbance was measured at 460 nm using a microplate reader (Varioskan LUX, Thermo Fisher Scientific, USA).

In vitro ROS-scavenging capacity of BPNs

Based on in vitro toxicity experiments, safe concentrations of BPNs (10, 30, 50, 100 μg/mL) were selected. RAW264.7 cells (2×10^4) were seeded in a 24-well plate and cultured for 12 h. Subsequently, after three PBS washes, LPS (5 μg/mL) was added to activate inflammatory macrophages, and the cells were concurrently treated with the aforementioned concentrations of BPNs. After 4 h, fresh medium containing 10% DCFH was added according to the ROS assay kit instructions. After 30 min, imaging was performed at Ex488/Em525 using an inverted fluorescence microscope scanner (ECLIPSE TS2, NIKON, Japan) under identical exposure conditions. Finally, ImageJ was used to quantify the average fluorescence intensity per field of view.

Preparation of HA-PBA

According to the preparation steps described by Qiao et al. [23], the synthesis of HA-PBA was structured as follows. HA (1 g, 2.5 mmol) was first dissolved in 100 mL of deionized water (Milli-Q, Millipore, USA), followed by the addition of EDC (575 mg, 3 mmol) and NHS (345 mg, 3 mmol). The pH of the solution was adjusted to 6 using a pH meter (Mettler Toledo, Switzerland). After stirring for 20 min on a magnetic stirrer (IKA, Germany), 3-aminophenylboronic acid (410.65 mg, 3 mmol) was added to the reaction system, and the pH was maintained at 9 using 1 M NaOH. The mixture was then allowed to react overnight at room temperature. The obtained product was purified by dialysis (molecular weight cutoff: 3500 Da, Spectrum Laboratories, USA) against deionized water for 3 days and subsequently freeze-dried using a LyoQuest-55 freeze dryer (Telstar, Spain) to yield the HA-PBA.

Preparation of GelMA hydrogel

Gelatin (5 g) was dissolved in PBS (pH 7.4, 50 mL) at 10% (w/v) under continuous stirring at 50 °C until completely dissolved. Subsequently, methacrylic anhydride (20 mL) was added dropwise to the gelatin solution, and the methacrylation reaction was carried out for 1 h under constant stirring. The resulting solution was dialyzed against deionized water using a dialysis membrane with a molecular weight cutoff of 12 kDa (Spectrum Laboratories, USA) for 5 days at room temperature and then lyophilized for 2 days using a freeze dryer (LyoQuest-55, Telstar, Spain) to obtain lyophilized GelMA.

Preparation and characterization of blank microneedles (MNs), BPNs@Microneedles (BMNs), NGF@Microneedles (NMNs), and BPNs&NGF@Microneedles (BNMNs)

Microneedles were fabricated using a multi-step molding strategy. Briefly, 0.03 g of lyophilized HA-PBA powder was dissolved in 1 mL of deionized water (containing 50 μg/mL BPNs) in three portions. After each addition, the mixture was vigorously stirred with a 1 mL pipette tip until complete dissolution. A ROS-responsive hydrogel precursor solution was then prepared by mixing 3% HA-PBA solution, 10% PVA solution, and deionized water at a ratio of 5:2:6. Separately, a photoinitiator lithium phenyl-2,4,6-trimethylbenzoylphosphinate (LAP) solution (8 mg/mL) and NGF dissolved in PBS was prepared and subsequently mixed with GelMA hydrogel to obtain a 15% solution (containing 50 ng/mL NGF), which was liquefied at 40 °C. In addition, a 250 mg/mL hydrogel solution for the backing layer was prepared. All three solutions were degassed by centrifugation at 3000 rpm

for 3 min. The ROS-responsive hydrogel precursor was then introduced into the cavities of a polydimethylsiloxane (PDMS) mold using a syringe with a trimmed tip, followed by a 2-min vacuum treatment in a vacuum drying oven to remove residual bubbles. The mold was then placed into a 50 mL centrifuge tube preloaded with a supporting layer and centrifuged at 4000 rpm for 3 min to ensure complete filling. Surface bubbles were removed by gentle scraping, and the mold was subsequently heated at 35 °C for 6 h to promote solidification. For shell formation, a metal spacer was placed on the negative mold, a resin-based positive mold was inserted, and the assembly was statically dried at 37 °C for 48 h. After drying, the positive mold was removed, and GelMA hydrogel solution was introduced into the cavities using a syringe with a trimmed tip. Vacuum treatment (2 min) and horizontal centrifugation (4000 rpm, 3 min) were applied as previously described to remove bubbles and ensure uniform filling. Finally, the mold was heated at 35 °C for 6 h to obtain the BPNs&NGF@Microneedles (BNMNs). Based on the above procedure, BPNs@Microneedles (BMNs), NGF@Microneedles (NMNs), and blank microneedles (MNs) were prepared in a manner consistent with the preparation of BNMNs. Specifically, for BMNs, a BPNs@HA-PBA solution (50 μg/mL) was prepared as described above and mixed with PVA and water to form the ROS-responsive hydrogel precursor solution. For NMNs, a NGF@GelMA hydrogel solution (containing 50 ng/mL NGF) was prepared using the same method and combined with HA-PBA, PVA solution, and water to form the final structure, identical to that of BNMNs. Blank microneedles (MNs) were prepared without BPNs or NGF, using only HA-PBA/PVA and GelMA hydrogel solutions. All preparation steps, including vacuum treatment, centrifugation, and heating for solidification, were performed to ensure that BMNs, NMNs, and MNs had similar structures and drug loading, allowing for experimental control comparisons. To minimize premature oxidation of BPNs during microneedle fabrication, freshly prepared BPN dispersions were stored in sealed containers at 4 °C and used immediately before preparation. The BPN-containing HA-PBA/PVA precursor was handled under reduced light exposure and processed as rapidly as possible.

Microneedle drug release detection

To evaluate the drug release from microneedles, they were immersed in PBS solutions containing different concentrations of H_2O_2 (10 μM and 100 μM) and enclosed in dialysis bags. The release of BPNs was quantified using inductively coupled plasma mass spectrometry (ICP-MS), while the release of NGF was measured by ELISA. The microneedles were incubated at 37 °C for a predetermined period, and the released amounts of BPNs and NGF were measured at specific time intervals to evaluate the temporal release profile under oxidative conditions.

Phosphate ion (PO_4^{3-}) concentration detection

1 mL of BPNs solution was added to a 5 mL reagent vial and incubated in a shaking incubator at 100 rpm and 37 °C for 7 days. Phosphate ions (PO_4^{3-}) were detected using a Malachite Green Phosphate Detection Kit. In brief, 200 μL of the test solution (BPNs or BNMNs) was mixed with 70 μL of the color reagent. After thorough mixing, the mixture was allowed to stand at room temperature for 30 min. The absorbance was recorded at 630 nm using a spectrophotometer (Thermo Fisher Scientific, USA). The phosphate concentration of the sample was calculated based on the standard curve and the dilution factor of the test sample.

H_2O_2 concentration detection

According to the instructions for the H_2O_2 detection kit, standard solutions were prepared at concentrations of 1, 5, 10, 20, 50, 100, and 200 μM in each well. Then, 100 μL of hydrogen peroxide detection reagent was added to each well. Absorbance was measured at 560 nm using a microplate reader (Thermo Fisher Scientific, USA).

Modeling of in vitro cellular systems

Sterilized microneedle systems were placed into DMEM medium without sodium pyruvate, L-alanine-L-glutamine, FBS, or P/S. H_2O_2 was added to achieve a concentration of 100 μM to simulate ROS in the inflammatory microenvironment. This concentration was selected based on previous studies showing that H_2O_2 is generated after nerve/tissue injury and participates in Schwann cell activation and axonal regeneration, and that 100 μM H_2O_2 is commonly used as a mild oxidative-stress stimulus in neural cell and peripheral nerve repair-related in vitro models [24, 25]. Based on drug release rates, sustained-release solutions from days 1 and 5 were selected as cell treatment groups. Sodium pyruvate (1.0 mM), L-pyruvate (2.05 mM), 10% FBS, or 1% P/S were then re-added to clear H_2O_2 and maintain cell culture. Finally, the supernatant was collected, filtered through a 0.22 μm membrane, and used as the extract for the corresponding group.

In vitro evaluation of the antioxidant and anti-inflammatory Effects of BNMNs

RAW264.7 cells (abbreviated as macrophages) act as a model for studying LPS-induced inflammatory responses in FNI. In the experiment, macrophages are treated with various ROS-responsive microneedle systems (MNs, BMNs, NMNs, and BNMNs) to observe changes in macrophage phenotype, particularly the transition from

M1 to M2 polarization. RAW264.7 cells were treated with LPS and the day-1 release extracts from different microneedle systems to evaluate inflammatory responses. mRNA was purified from lysed cells, reverse-transcribed, amplified, and quantified using a real-time PCR system. For flow cytometry analysis, macrophages were washed, fixed, and then incubated with anti-CD86 or anti-CD206 antibodies. Finally, they were analyzed using a Beckman Coulter flow cytometer (BD Fortessa, New Jersey, USA). The concentrations of TNF-α and IL-10 in the supernatant were measured using an ELISA kit according to the manufacturer's instructions.

In vitro evaluation of the antioxidant and anti-inflammatory mechanisms of BNMNs

Given the exceptional antioxidant and anti-inflammatory properties of BNMNs, we commissioned Shanghai Paisenuo Biotechnology Co., Ltd. to perform RNA sequencing (RNA-seq), including mRNA enrichment, library preparation, and sequencing. After data cleaning, high-quality RNA sequencing data were obtained for the analysis of LPS-induced RAW264.7 cells and LPS-induced RAW264.7 cells treated with the supernatant (1 day) released by BNMNs. Briefly, RAW264.7 cells (5 million per tube) were treated for 12 h and collected using Trizol reagent (Invitrogen, USA). The cleaned data provided by Paisenuo Biotechnology Co., Ltd. were then analyzed using R software (version 4.3.3). The RNA-seq clean data are provided in the Supplementary File, and the analysis workflow and visualization methods followed those of previous studies [26]. Key genes identified in pathways uncovered by transcriptome sequencing were validated by Western blot. In brief, proteins were separated on a 10% SDS-PAGE gel and subsequently transferred to a polyvinylidene fluoride (PVDF) membrane. After incubation with 4% skim milk for 1.5 h, the membrane was incubated overnight at 4 °C with the primary antibody. The membrane was incubated with the secondary antibody for 1 h, then washed three times with TBST. Fluorescent signals were detected using an Odyssey imaging system (Tanon, Shanghai, China).

Evaluation of the performance of BNMNs in promoting neural repair

To evaluate the neuro-regenerative capacity of BNMNs, PC12 and RSC96 cells were employed as in vitro models for neural differentiation and repair. The cells were treated with various microneedle systems, including MNs, BMNs, NMNs, and BNMNs, to observe their effects on cell morphology, neurite outgrowth, and gene expression related to neural regeneration. The experiment was set up with the following groups: G1 group (Control): Untreated PC12/RSC96 cells, serving as the baseline control; G2 group (H_2O_2): PC12/RSC96 cells treated with the supernatant from which H_2O_2 had been removed; G3 group (MNs): PC12/RSC96 cells treated with H_2O_2-induced MNs; G4 group (BMNs); PC12/RSC96 cells treated with H_2O_2-induced BMNs; G5 group (NMNs): PC12/RSC96 cells treated with H_2O_2-induced NMNs; G6 group (BNMNs): PC12/RSC96 cells treated with H_2O_2-induced BNMNs. CCK-8 assay and Calcein/PI kits were used to determine the effects of BNMNs on the cellular viability of PC12 and RSC96 cells at day 5. Neurite outgrowth was measured by Phalloidin/DAPI staining, where Phalloidin was used to label F-actin in neurites, and DAPI stained the cell nuclei, followed by fluorescence microscopy to assess neurite length and branching. Parallel cell samples were collected for quantitative analysis of Tubb3, Gap43, and Map2 expression via real-time quantitative PCR (RT-qPCR). mRNA was purified from lysed cells, reverse-transcribed, amplified, and quantified using an RT-qPCR system. The $2^{-\Delta Ct}$ method was used to evaluate the relative expression levels. Western blot was used to measure the expression levels of TRKA, p-TRKA, AKT, p-AKT, ERK, p-ERK, CREB, and p-CREB, key markers of neurotrophic signaling involved in neural repair. In addition, the concentrations of NGF, BDNF, and VEGFA in the supernatant of RSC96 cells were measured using an ELISA kit according to the manufacturer's instructions.

The effects of different treatments on RSC96 Schwann cell proliferation, migration, and paracrine-mediated angiogenesis were systematically evaluated. Briefly, RSC96 cells were seeded in culture plates and treated with different formulations or corresponding extracts according to the experimental grouping. Cell proliferation was assessed using an EdU incorporation assay. After treatment, cells were incubated with EdU working solution, fixed with 4% paraformaldehyde, permeabilized with Triton X-100, and stained according to the manufacturer's instructions. Nuclei were counterstained with DAPI, and the EdU-positive cell ratio was calculated as the percentage of EdU-positive nuclei among total DAPI-stained nuclei. The migratory capacity of RSC96 cells was evaluated using Transwell and wound healing assays. For the Transwell assay, RSC96 cells suspended in serum-free medium were seeded into the upper chambers, while medium containing different formulations or corresponding extracts was added to the lower chambers. After incubation, migrated cells on the lower membrane surface were fixed, stained with crystal violet, imaged, and quantified by counting stained cells in randomly selected fields. For the wound healing assay, confluent RSC96 monolayers were scratched with a sterile pipette tip, washed with PBS, and cultured with different treatment media. Images were captured at 0, 6, and 24 h, and the migration rate was calculated based on the reduction in wound area. To assess paracrine-mediated

angiogenesis, conditioned media were collected from RSC96 cells after different treatments, centrifuged to remove cellular debris, and used for HUVEC tube formation assays. In addition, the levels of NGF, BDNF, and VEGFA in the conditioned media were detected using ELISA kits according to the manufacturer's protocols. For the tube formation assay, Matrigel was added to precooled 96-well plates and allowed to polymerize at 37 °C. HUVECs suspended in the corresponding RSC96-conditioned media were seeded onto the Matrigel-coated wells and incubated at 37 °C with 5% CO_2. Capillary-like structures were photographed under an inverted microscope, and angiogenic parameters, including the number of nodes, total tube length, and total branching length, were quantified using ImageJ software with the Angiogenesis Analyzer plugin.

Facial nerve crush injury model and treatment

All animal procedures were reviewed and approved by the Institutional Animal Care and Use Committee of Tongji University (Approval Number: SHDSYY-2025-P1817-2), in compliance with the ARRIVE guidelines [27]. Prior to the experiments, sample size estimation was performed using the degree of freedom (E value) method [28]. Eight-week-old female C57BL/6 mice were purchased from the Animal Center of the Tenth People's Hospital Affiliated to Tongji University (Shanghai, China) and housed under specific pathogen-free (SPF) conditions maintained at 20–25 °C, 40–70% humidity, and a 12-h light-dark cycle. All mice had free access to autoclaved pellet feed and drinking water. Mice were acclimated to the environment for 1 week before experimentation. All surgeries were performed under anesthesia with 1.25% tribromoethanol (200 μL/10 g body weight). Using aseptic technique, the right facial nerve was exposed at its exit from the mastoid foramen in each animal. The nerve was compressed twice at different angles (30 s each) using jewelry forceps. Postoperatively, the wound was closed, and the animals recovered on a heated blanket. Sham-operated mice served as controls. The same surgeon performed all procedures to minimize inter-animal variation. Following injury, all mice were randomly assigned to 6 distinct experimental groups, with 12 mice per group. The 800-μm microneedle systems were divided into four groups (MNs, BMNs, NMNs, and BNMNs), sterilized with 75% ethanol, and irradiated with ultraviolet light for 24 h.

To verify whether the nerve growth factor (NGF) released by the microneedle system could reach the local microenvironment of the FNI, tissue samples were collected from the injured facial nerve and the surrounding area following microneedle application. In brief, on day 7, mice in the different treatment groups were euthanized, and the local tissue surrounding the injured facial nerve was carefully harvested, weighed, and homogenized in cold PBS containing protease inhibitors. Following centrifugation, the supernatant was collected, and NGF concentrations were determined using an ELISA kit according to the manufacturer's instructions. NGF levels were normalized by tissue weight and expressed in pg/mg of tissue. Electrophysiological assessment was performed at day 7 to objectively evaluate facial nerve functional recovery. Mice were anesthetized, and the injured facial nerve was exposed. A stimulating electrode was placed proximal to the injury site, and recording electrodes were inserted into the ipsilateral orbicularis oculi. Supramaximal electrical stimulation was applied to the facial nerve, and evoked compound muscle action potential-like responses were recorded using an electrophysiological recording system. The peak-to-peak amplitude of the evoked response was quantified as an indicator of functional axonal recovery. All electrophysiological recordings and analyses were performed by investigators blinded to the treatment groups.

Penetration ability of the BNMNs patch

The BNMNs patches were pressed onto the injured site in mice, followed by moistening with saline for better attachment to the skin. The patch was removed 3 days after application to examine the punctures. Meanwhile, skin samples with attached MNs were fixed in 4% paraformaldehyde (PFA), dehydrated in ethanol, and processed into 10 μm paraffin sections for hematoxylin and eosin (H&E) staining.

Assessment of functional recovery

Facial nerve crush injury results in loss of blink reflex, abnormal vibrissae movement, and abnormal vibrissae direction. Postoperatively, observations were conducted three times per week, and vibrissae movement and blink reflex were recorded in each group. The blink reflex was assessed by blowing air toward the eyelid from a distance of approximately 3 cm using a 5-mL syringe. As described previously [29], eyelid closure and whisker function were evaluated in each mouse according to the following criteria: 3 = no detectable movement; 2 = detectable movement; 1 = marked but asymmetrical spontaneous movement; 0 = symmetrical spontaneous movement. In addition, an extra criterion was introduced: 1 = the nasal tip deviates contralaterally; 0 = the nasal tip is centered. The neurological function score was calculated by summing all individual scores. All behavioral assessments, including vibrissae movement and blink reflex evaluation, were performed by investigators blinded to the treatment group allocation.

In vivo toxicity

After 14 days, the animals were euthanized, and their hearts, livers, spleens, lungs, and kidneys were collected

for H&E staining to assess the potential systemic toxicity of different microneedle systems. Furthermore, the following parameters were measured: hemoglobin (HGB), red blood cells (RBC), platelets (PLT), white blood cells (WBC), lymphocytes (LYM), monocytes (MON), neutrophils (NEUT), aspartate transaminase (AST), alanine transaminase (ALT), blood urea (UREA), and blood urea nitrogen (BUN) levels.

Histopathological evaluation and immunohistochemical analysis

Mice were euthanized by carbon dioxide inhalation, and the facial nerve tissues were freshly harvested and immediately fixed in 4% paraformaldehyde. After fixation, the tissues were subjected to routine dehydration, clearing, and paraffin embedding, and subsequently sectioned into 5-μm-thick slices for histological and immunohistochemical analyses. To evaluate the in vivo antioxidant and anti-inflammatory effects of BNMNs, a subset of facial nerve samples was processed for cryosectioning, and intracellular reactive oxygen species (ROS) levels were analyzed. For immunofluorescence staining, the tissue sections were incubated with primary antibodies against inducible nitric oxide synthase (iNOS) and CD206 to assess macrophage polarization. After thorough washing and incubation with appropriate fluorescently labeled secondary antibodies, the sections were visualized using a laser scanning confocal microscope. To further investigate ultrastructural changes associated with nerve injury and regeneration, TEM was performed to examine the facial nerve architecture. Myelin thickness was quantified by averaging the maximal and minimal diameters, and the myelination index (G-ratio) was calculated to evaluate the extent of demyelination and remyelination. In parallel, representative paraffin-embedded nerve sections were subjected to immunohistochemical analysis using antibodies against myelin basic protein (MBP, 1:500) and S100β (1:1000) to assess myelin formation and Schwann cell distribution. Fluorescence images were acquired using a fluorescence microscope, and the proportion of positively stained cells was quantitatively analyzed using ImageJ software. Finally, Luxol Fast Blue (LFB) staining was performed to further evaluate myelin integrity and regeneration in the facial nerve tissue. This analysis provided morphological evidence of myelination status and Schwann cell–associated remyelination, serving as a complementary assessment to immunostaining and ultrastructural observations and enabling a comprehensive evaluation of nerve regeneration and repair.

Statistical analyses

Data were analyzed using GraphPad Prism 9.0 and R (v4.3.3). Results are presented as mean ± standard deviation (SD). For comparisons between two groups, an unpaired two-tailed Student's t-test was used. For comparisons among three or more groups, one-way ANOVA followed by Tukey's post hoc test was applied unless otherwise stated. For RNA-seq, p values were adjusted for multiple testing using the Benjamini–Hochberg false discovery rate (FDR) procedure.

Results and discussion

Preparation and characterization of BPNs and double-layer microneedle system

Fabrication of the ROS-responsive BPNs/NGF-loaded core-shell microneedles (BNMNs) began by preparing the outer shell layer using a combination of the ROS-responsive hydrogel HA-PBA/PVA and BPNs. The inner shell layer was formed by incorporating NGF into GelMA hydrogel. The microneedle patch fabrication involved a multi-step mold-casting approach, integrating vacuum treatment, centrifugation, and heating to ensure uniform filling and eliminate bubbles. Following these steps, the microneedle patches underwent dehydration and mold separation, yielding BNMNs capable of time-controlled drug release (Fig. 1A). The BPNs were synthesized via liquid-phase exfoliation, and their structural characteristics were comprehensively evaluated using various analytical techniques. TEM images revealed that the BPNs exhibited irregular, multi-shaped structures with slightly undulating edges, consistent with mechanical exfoliation, and energy-dispersive X-ray spectroscopy (EDS) mapping showed the expected phosphorus signal together with carbon/background elements from the support (Fig. 1B). Further structural analysis was performed using SEM and AFM. The SEM image clearly illustrated the morphology and structure of the BPNs (Fig. 1C), while the AFM image confirmed the successful exfoliation of BPNs flakes (Fig. 1D).

The AFM image revealed irregular flake-like or granular structures that appear bright yellow/white against a purple background, indicating significant protrusion above the substrate surface. These particles were dispersed relatively independently, with no large-area aggregation or continuous film formation, demonstrating excellent dispersion. The size distribution of the BPNs was determined by dynamic light scattering (DLS), revealing a mean particle size of approximately 260.3 ± 12.5 nm and a zeta potential of -24.39 ± 3.2 mV (Fig. 1E), confirming their uniformity. Infrared spectroscopy provided the following insights: (1) A characteristic peak in the 500–600 cm^{-1} range corresponds to the out-of-plane bending vibration of the P-P bond in black phosphorus nanosheets, reflecting the vertical vibration of interlayer phosphorus atoms; (2) A peak in the 700–800 cm^{-1} range is attributed to the in-plane bending vibration of the P-P bond, related to the cooperative in-plane vibration of phosphorus atoms; (3) A broad peak in the

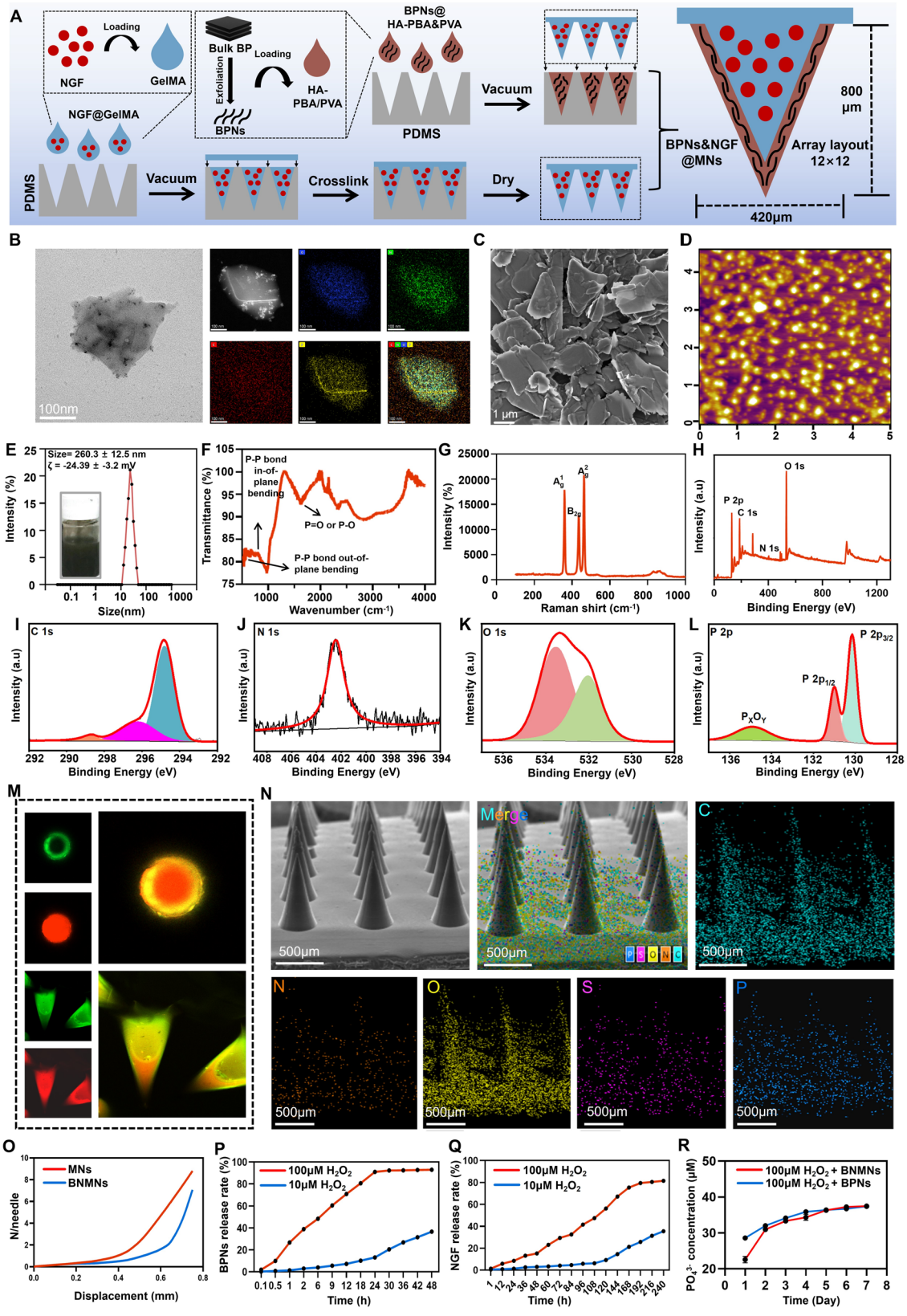

Fig. 1 (See legend on next page.)

(See figure on previous page.)

Fig. 1 Preparation and characterization of the BPNs and double-layer BNMNs. (**A**) Schematic illustration of the fabrication process of BNMNs. (**B**) Transmission electron microscopy (TEM) images of BPNs. Energy-dispersive X-ray spectroscopy (EDS) elemental map shows the distribution of elements (C: Carbon, N: Nitrogen, P: Phosphorus). (**C**) Scanning electron microscope (SEM) image of BPNs. (**D**) Atomic force microscopy (AFM) image showing the surface structure of BPNs. (**E**) Zeta potential and particle size distribution. (**F**) Fourier-transform infrared spectroscopy (FTIR). (**G**) Raman spectra. (**H**) X-ray photoelectron spectroscopy (XPS) analysis showing the chemical states of BPNs. (**I**) C 1s, (**J**) N 1s, (**K**) O 1s, and (**L**) P 2p XPS spectrum. (**M**) Fluorescence microscopy images. **(N)** SEM images of BNMNs, and the right EDS elemental map indicates the distribution of elements (C: Carbon, N: Nitrogen, O: Oxygen, S: Sulfur, P: Phosphorus). (**O**) Mechanical properties. Release curves of (**P**) BPNs and (**Q**) NGF over time under H_2O_2 (100 μM and 10 μM) conditions. (**R**) Phosphate ion (PO_4^{3-}) concentration changes over time

1500–1700 cm^{-1} range is attributed to surface oxidation or adsorbed species (such as P = O or P-O bonds), resulting from the reaction of black phosphorus nanosheets with oxygen or water (Fig. 1F). The Raman spectrum showed distinct peaks in the 200–600 cm^{-1} range (Fig. 1G), corresponding to the superposition of these three modes, with the A_g^2 mode (466 cm^{-1}) as the main peak. This indicates that the sample possesses a highly ordered layered structure. The sharp and high-intensity peaks further suggest that the black phosphorus has good crystallinity and few lattice defects. These infrared spectral features confirm the characteristic vibrational modes of BPNs. XPS analysis further corroborated the chemical composition of the BPNs, revealing the presence of phosphorus (P), oxygen (O), and nitrogen (N), in line with the expected molecular structure (Fig. 1H and K). The binding energy peaks associated with phosphorus (P 2p) provided additional evidence for the oxidation states of the BPNs, confirming their successful synthesis (Fig. 1L). Collectively, these results validate the successful preparation of BPNs and their uniform dispersion.

To determine the optimal drug-loading concentration for BPNs, first, CCK-8 and ROS assays were conducted to assess toxicity and ROS-scavenging capacity. CCK-8 results indicated that BPNs at concentrations ranging from 0 to 50 μg/mL maintained over 90% cellular viability after 24 h of treatment (Figure S1A). ROS detection images and statistical analysis revealed that BPNs at 50 μg/mL exhibited excellent ROS scavenging activity, while ROS levels significantly increased in macrophages treated with 100 μg/mL BPNs, indicating a dose-dependent toxicity (Figures S1B and S1C). Similarly, CCK-8 assay results confirmed that NGF exhibited broad safety for macrophages. After 24 h of exposure to NGF at concentrations ranging from 0 to 200 ng/mL, macrophage survival rates remained above 90% (Figure S2). Based on previous studies and therapeutic relevance, 100 ng/mL NGF was selected as the optimal concentration for treating FNI in mice [30]. NGF was subsequently incorporated into the core of the microneedles, which were fabricated using GelMA hydrogel to achieve sustained release. The BNMNs were characterized via SEM (Figure S3A–S3C). The SEM images revealed a well-defined conical shape, with a height of 800 μm and a base diameter of 420 μm, arranged in a 12 × 12 array. These features suggest precise and uniform microneedle fabrication, which is critical for effective drug delivery and tissue regeneration applications. To visualize the bilayer structure of the microneedles, HA-PBA/PVA was labeled with rhodamine (RHO), while the base layer of GelMA solution was mixed with fluorescein isothiocyanate (FITC). Signal distribution analysis showed that RHO was evenly distributed from the base to the tip of the microneedle, while FITC was primarily localized to the base layer (Fig. 1M). To better evaluate the synergistic therapeutic performance of BNMNs, blank microneedles (MNs), BPNs-loaded microneedles (BMNs), and NGF-loaded microneedles (NMNs) were prepared. SEM images of these microneedle systems are shown in Figure S4A–S4C. EDS analysis revealed distinct elemental compositions for each microneedle type. Blank microneedles (MNs) contained only carbon (C), nitrogen (N), and oxygen (O), while BPNs-loaded microneedles (BMNs) lacked sulfur (S) and NGF-loaded microneedles (NMNs) lacked phosphorus (P). In contrast, BPNs- and NGF-loaded microneedles (BNMNs) contained C, N, O, S, and P, uniformly distributed throughout the microneedle structure, confirming successful incorporation of BPNs and NGF (Figure S5A–S5C and Fig. 1N). Mechanical testing revealed that blank MNs exhibited a force of approximately 9 N per needle at a displacement of about 0.7 mm. In comparison, BNMNs demonstrated a reduced force of approximately 5 N per needle under the same conditions (Fig. 1O). However, the force required for microneedle penetration of the stratum corneum typically ranges between 0.1 N and 0.3 N. Thus, although the mechanical properties of BNMNs were lower than those of blank MNs, they still exceeded the minimum threshold required for skin penetration, ensuring effective transdermal drug delivery [31]. This enhanced mechanical performance is crucial for successful in vivo applications, where efficient skin penetration and drug release are paramount. The drug release profiles of BPNs and NGF from the microneedles were measured under various conditions. The release of BPNs was significantly accelerated under 100 μM H_2O_2 compared to 10 μM H_2O_2 (Fig. 1P), indicating that BPNs were responsive to ROS levels, which is essential for treating oxidative stress in nerve injury environments. In contrast, NGF release from BNMNs exhibited a slower, more sustained release pattern (Fig. 1Q). Compared with free BPNs, which released higher concentrations of PO_4^{3-} (approximately 32 μM) within 24 h, BNMNs released higher

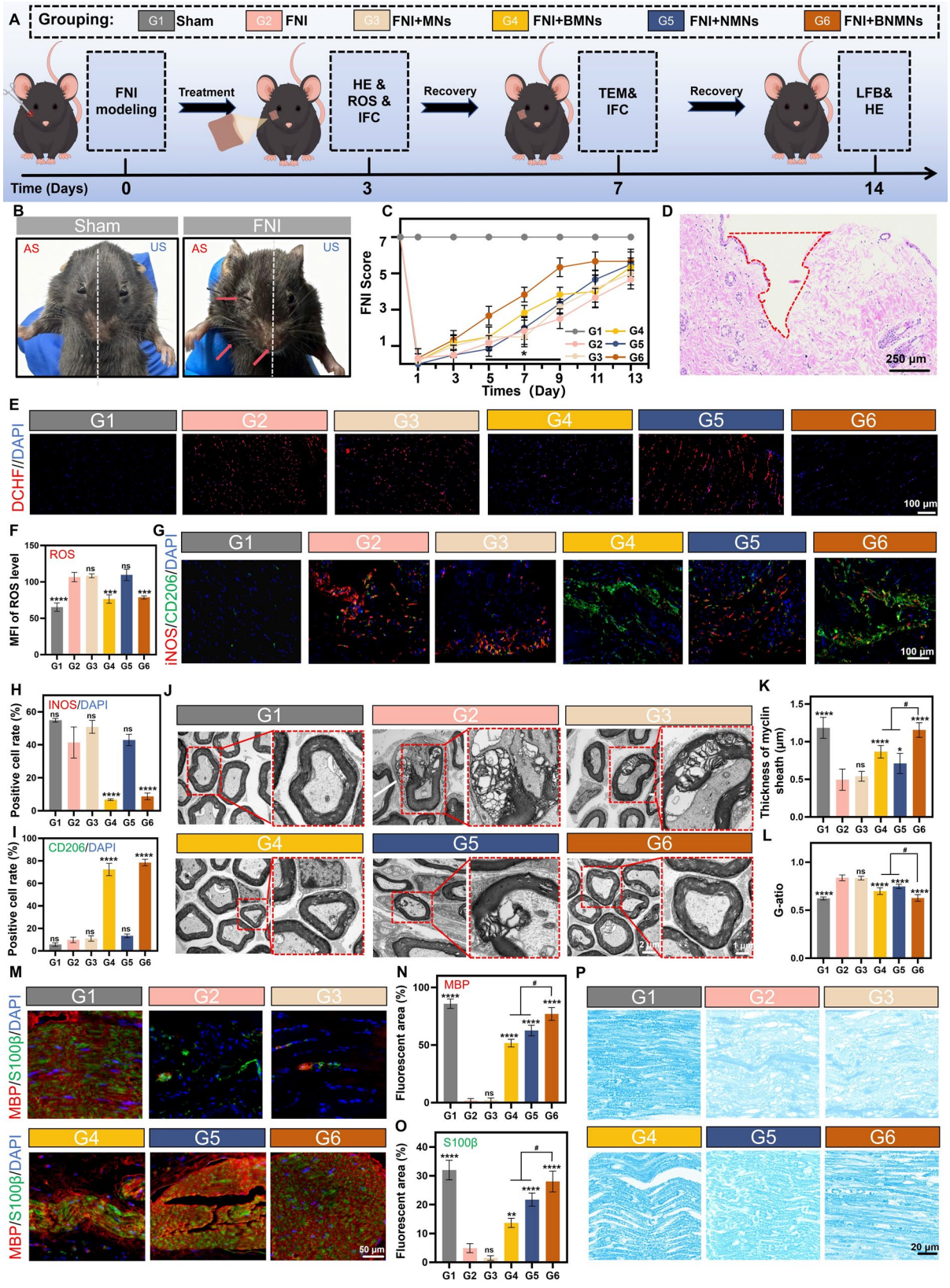

Fig. 2 (See legend on next page.)

(See figure on previous page.)

Fig. 2 Evaluation of the therapeutic efficacy of BPNs in vivo based on the FNI model. (**A**) Schematic illustration of the treatment process for the facial nerve crush injury model. (day 0: Facial nerve crush surgery was performed and treatment intervention was administered to the respective groups; day 3: The first treatment assessment; day 7: The second treatment assessment; day 14: The final treatment assessment and safety assessment). (**B**) Representative clinical manifestations in the sham surgery group and FNI model group. (**C**) FNI scores across different groups during the treatment process ($n = 12$). Mice were divided into different groups: G1 (SHAM) group, G2 (FNI) group, G3 (FNI + MNs) group, G4 (FNI + BMNs) group, G5 (FNI + NMNs) group, and G6 (FNI + BNMNs) group. (**D**) Representative hematoxylin and eosin (H&E) staining of BNMNs therapy. (**E**) Representative image of DCFH staining in facial nerve tissue and (**F**) statistical results for mean fluorescence intensity (MFI) ($n = 3$). (**G**) Representative image of iNOS- and CD206-positive cells in facial nerve tissue and **(H, I)** statistical results for MFI ($n = 3$). (**J**) Representative TEM images of FNI, alongside statistical results for (**K**) myelin thickness and (**L**) G-ratio measurements ($n = 12$). (**M**) Representative immunofluorescent images of transverse sections of the regenerated nerves double-stained for S100β (red)/MBP (green) and **(N, O)** statistical results for fluorescent area ($n = 3$). (**P**) Luxol Fast Blue (LFB) staining of facial nerve tissue. Data are presented as mean ± SD. Statistical significance: ns, not significant; *$p < 0.05$, **$p < 0.01$, ***$p < 0.001$, ****$p < 0.0001$ compared with G2 group; #$p < 0.05$ compared with G6 group

concentrations of PO_4^{3-} (approximately 31 μM) over 48 h, which is beneficial for subsequent neural repair (Fig. 1R). Notably, the ROS-triggered burst release of BPNs precedes the sustained diffusion-controlled release of NGF, establishing a sequential therapeutic window in which early redox–inflammatory remodeling is followed by prolonged neurotrophic support.

In vivo evaluation of therapeutic efficacy of BPNs in the FNI model

To evaluate the therapeutic potential of BNMNs in nerve regeneration, an FNI model in mice was employed, which is widely used to mimic nerve damage caused by traumatic or surgical injuries [29]. The experimental groups are as follows: G1 group: Sham-treated group for comparison; G2 group: FNI group with no treatment; G3 group: FNI treated with blank MNs; G4 group: FNI treated with BMNs; G5 group: FNI treated with NMNs; G6 group: FNI treated with BNMNs. In this model, typical symptoms, including eyelid paralysis, whisker movement defects, and mouth drooping, were observed (Fig. 2B) [3]. The therapeutic effects of different treatment regimens were assessed at several time points (days 1, 3, 5, 7, 10, and 13) following treatment. The G6 group, which received a combination of NGF-loaded and BPN-loaded microneedles, exhibited the most significant functional recovery compared to the G2 group (Fig. 2C). From day 5 to day 11, the G6 group demonstrated significantly higher motor function scores, indicating accelerated recovery of facial nerve function. These results indicate that BNMNs outperform single-component microneedles, supporting the necessity of sequential antioxidation and neurotrophic signaling rather than either intervention alone. This enhanced recovery is likely due to the combined effects of NGF and BPNs, which promote nerve regeneration and alleviate nerve injury symptoms. This finding is consistent with prior reports showing that NGF supports neuronal survival and regeneration, while BPNs, with their antioxidant properties, help reduce oxidative stress, a factor known to impede nerve repair [16, 17]. The combination therapy in the G6 group thus appears to synergistically accelerate motor function recovery after FNI.

Based on the efficacy of BNMNs in improving FNI recovery, days 3, 7, and 14 were selected to systematically investigate the sequential effects of BNMNs on antioxidant and neuroprotective mechanisms. Oxidative stress and inflammation are key factors in nerve injury and repair. To assess the impact of different treatments on these processes, ROS levels were measured using 2′,7′-dichlorofluorescein (DCF) staining [32]. The FNI model demonstrated significant ROS generation, indicative of oxidative stress at the injury site (Fig. 2E). However, while treatments with microneedles (G3, G5) had limited effects on ROS clearance, the G4 and G6 groups showed a marked reduction in ROS levels (Fig. 2F). This suggests that BPNs are effective at reducing oxidative stress, a critical step in enhancing nerve regeneration. Additionally, immunofluorescence staining was performed for inflammation-related markers. After FNI injury, M1-type pro-inflammatory macrophages were recruited to the injury site, exacerbating the damage (Fig. 2G). In contrast, treatment in the G4 and G6 groups significantly reduced the proportion of M1 macrophages, while promoting the polarization of M2 macrophages, which are known to facilitate tissue repair (Fig. 2H and I). This shift from the pro-inflammatory M1 phenotype to the repair-promoting M2 phenotype is crucial for creating a favorable microenvironment for nerve regeneration [33]. Consistent with ROS scavenging, BPNs-containing microneedles suppressed M1-like activation and promoted M2-like polarization at the lesion site, suggesting that redox remodeling directly contributes to inflammatory resolution and a permissive regenerative niche.

To further verify whether NGF released from the microneedle system could reach the local FNI microenvironment, NGF levels in tissue homogenates collected from the FNI/perineural region were quantified by ELISA on day 7 across the different treatment groups. NGF-containing microneedle groups showed markedly higher local NGF levels than non-NGF groups, with the highest NGF level observed in the G6 group (Figure S6). These results provide direct biochemical evidence that NGF released from BNMNs can reach and be retained within the perineural microenvironment after microneedle

application, thereby supporting the subsequent neurotrophic effects observed during nerve repair. To determine whether this localized NGF delivery translated into functional recovery at the tissue level, electrophysiological assessment was performed at day 7 after injury. Representative evoked muscle compound potential (EMCP) waveforms were recorded from facial muscles following facial nerve stimulation (Figure S7A), and the EMCP amplitude was quantitatively analyzed (Figure S7B). Compared with the FNI group (G2), all treatment groups exhibited partial recovery of electrophysiological function. However, the G3 group (blank MNs) showed no significant improvement, while the G5 group (NGF-loaded microneedles) exhibited only modest recovery, indicating that NGF alone was insufficient to fully restore functional nerve conduction in the presence of a ROS-rich microenvironment. In contrast, the G4 group (BPNs-loaded microneedles) demonstrated improved EMCP amplitude, supporting the importance of oxidative stress clearance in facilitating nerve repair. Notably, the G6 group (BNMNs) exhibited the highest EMCP amplitude among the injured groups, suggesting that the combination of early ROS scavenging and subsequent NGF-mediated neurotrophic support more effectively promotes functional axonal recovery and muscle reinnervation.

Histological evaluations performed on day 7 further confirmed the therapeutic effects of the treatments. TEM images revealed significant differences in nerve regeneration among the treatment groups (Fig. 2J). In both the G2 and G3 groups, fragmented myelin with an onion-like appearance was observed, indicating successful establishment of the FNI model. This pathological change suggests significant demyelination, which is a characteristic feature of nerve injury. Furthermore, this model provides a reliable foundation for evaluating the effectiveness of therapeutic interventions that promote remyelination and nerve regeneration. The G6 group exhibited the thickest myelin sheaths and the lowest G-ratio, both of which are indicative of successful nerve regeneration (Fig. 2K and L). In contrast, the G4 and G5 groups exhibited minimal regeneration, characterized by thinner myelin sheaths and disorganized axonal structures. The increased myelin thickness suggests robust remyelination, while the lower G-ratio indicates an optimal balance between axonal size and myelin sheath thickness, a hallmark of efficient nerve repair. These findings suggest that the combination of BPNs- and NGF-loaded microneedles significantly enhanced nerve repair compared to other treatment strategies. Immunofluorescence staining for S100β and MBP, markers for Schwann cells and myelination, respectively, corroborated the TEM results [34]. The G6 group showed higher levels of both S100β and MBP expression, further confirming that the combination therapy promoted Schwann cell differentiation and myelination, key steps in peripheral nerve regeneration (Fig. 2M and O). Finally, LFB staining on day 14 highlighted the myelin structures, with apparent differences observed between the groups (Fig. 2P). In the G1 group, intact myelin sheaths were present, while in the G2 and G3 groups, significant demyelination was observed, indicating nerve injury. The G4 and G5 groups show some signs of remyelination, with partial recovery of myelin integrity. The G6 group exhibited the most pronounced remyelination and the best-organized myelin sheaths.

Collectively, these results suggest that BNMNs facilitate peripheral nerve repair through a coordinated and stage-specific therapeutic mechanism. Early after injury, BPNs released from the microneedle shell effectively attenuate oxidative stress and modulate the inflammatory microenvironment by reducing M1-like macrophage activation while promoting M2-like polarization. This redox remodeling appears to establish a permissive niche for subsequent regeneration. Following this initial phase, sustained NGF release from the microneedle core is retained within the perineural region, providing localized neurotrophic support. Functional electrophysiological assessment further indicates that NGF alone confers limited recovery in a ROS-rich environment, whereas the combination strategy significantly enhances axonal conduction and muscle reinnervation. Consistently, histological analyses, including TEM, immunofluorescence staining, and LFB staining, demonstrate improved myelination, reduced G-ratio, and better structural organization in the BNMNs group compared with single-component treatments. Together, these findings support the concept that sequential antioxidative regulation followed by neurotrophic stimulation is more effective than either strategy alone, highlighting the importance of temporally programmed intervention in peripheral nerve regeneration.

In Vivo Biocompatibility of BNMNs

The biosafety of microneedles is crucial for clinical applications [35]. To evaluate the in vivo biocompatibility of BNMNs, H&E staining was performed on the hearts, livers, spleens, lungs, and kidneys of mice after 14 days of different treatments. Additionally, blood samples were collected for biochemical analysis to assess liver and kidney function and to further evaluate the safety profile of BNMNs (Fig. 3A).

The body weights of mice in different treatment groups were measured every two days. The results indicated that microneedle treatment did not affect the mice's eating and drinking behaviors (Fig. 3B). In the FNI model, a decrease in body weight was observed on the third day post-surgery, likely due to the surgical procedure and anesthesia. Over time, the body weight of the mice

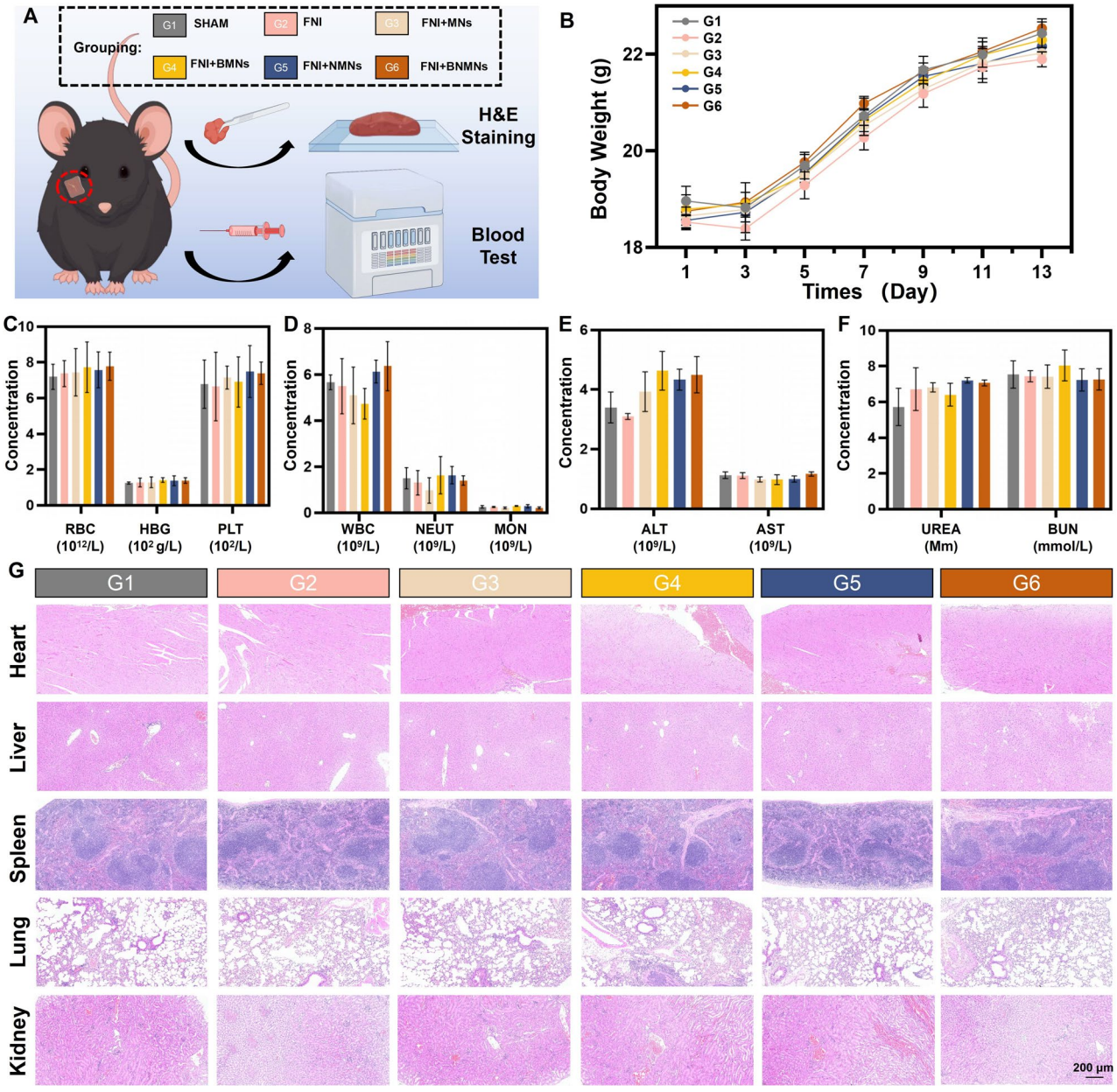

Fig. 3 Safety evaluation of BPNs in the FNI model. (**A**) Experimental design for safety evaluation of the BPNs used in the FNI model. (**B**) Body weight changes across the 13-day experimental period for all groups. (**C, D**) Hematological analysis, (**E**) liver function, and (**F**) kidney function of FNI model mice with different treatments. (**G**) Representative H&E-stained images of major organs under various conditions. Data are presented as mean ± SD ($n = 3$)

gradually recovered, reaching near baseline levels, which suggests that the BNMNs treatment did not have a significant adverse impact on the mice's general health and behavior. Further hematological analysis revealed no abnormal changes in the blood parameters across all treatment groups, including red blood cells (RBC), hemoglobin (HGB), platelets (PLT), white blood cells (WBC), neutrophils (NEUT), and monocytes (MON) (Fig. 3C and D). Additionally, liver (ALT, AST) and kidney (urea, BUN) biomarkers did not show any significant deviations, reinforcing the safety of BNMNs treatment (Fig. 3E and F). Finally, H&E staining confirmed the absence of any observable damage or inflammation in the primary organs, including the heart, liver, spleen, lungs, and kidneys, across all treatment groups (Fig. 3G). These findings collectively suggest that BNMNs possess favorable short-term biocompatibility, supporting further preclinical evaluation.

In conclusion, through a series of in vivo safety evaluations, BNMNs were shown to have no significant adverse effects on the physiological and biochemical parameters

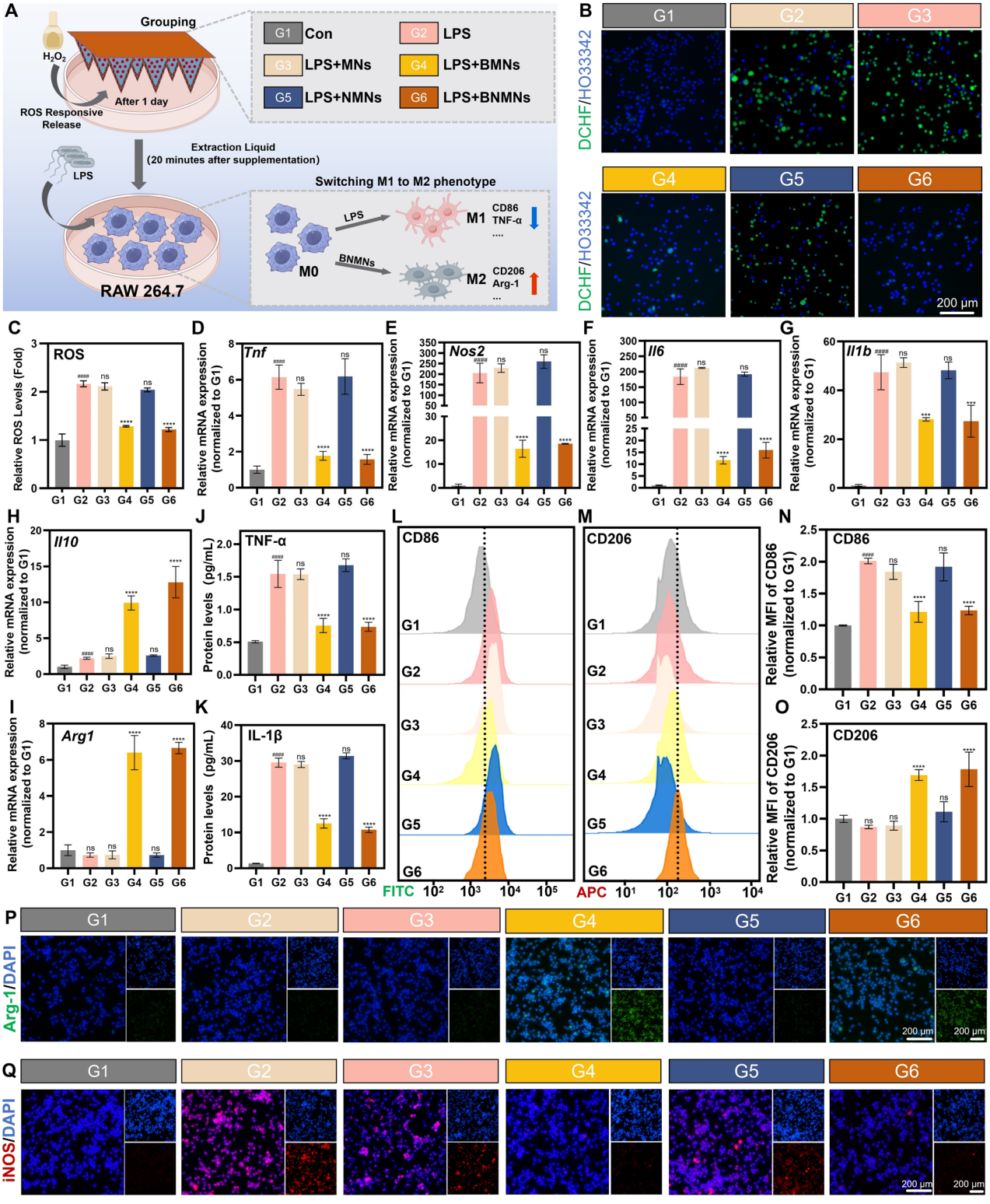

Fig. 4 (See legend on next page.)

(See figure on previous page.)

Fig. 4 ROS-responsive BNMNs mediated the reprogramming of RAW264.7 cells (abbreviated as macrophages) towards the M2 phenotype. (**A**) Schematic illustration of the experimental design. The experimental design was divided into six groups: Control (G1), LPS (G2), LPS + MNs (G3), LPS+BMNs (G4), LPS+NMNs (G5), and LPS+BNMNs (G6). (**B**) Representative DCFH-DA staining images showing intracellular ROS generation across groups (green: ROS; blue: nuclei stained with Hoechst 33342). (**C**) Quantification of intracellular ROS levels. Relative mRNA expression levels of (**D**) *Tnf*, (**E**) *Nos2*, (**F**) *Il6*, (**G**) *Il1b*, (**H**) *Il10*, and **(I)** *Arg1* measured by qRT-PCR. Protein secretion levels of (**J**) TNF-α and (**K**) IL-1β measured by ELISA. **(L, M)** Flow cytometry analysis of surface markers CD86 (M1) and CD206 (M2) expression. (**N, O**) Quantification of the relative mean fluorescence intensity (MFI) of CD86 and CD206 normalized to G1. (**P**) Representative immunofluorescence images of Arg-1 (green) and (**Q**) iNOS (red) expression with DAPI nuclear counterstaining (blue). Data are presented as mean ± SD ($n = 3$). Statistical significance: ns, not significant; *$p < 0.05$, ** $p < 0.01$, *** $p < 0.001$, **** $p < 0.0001$ compared with G2 group; $^{\#}p < 0.05$, $^{\#\#}p < 0.01$, $^{\#\#\#}p < 0.001$ and $^{\#\#\#\#}p < 0.0001$ compared with G1 group

of the mice. These results establish a strong foundation for the clinical application of BNMNs in biomedicine.

In vitro therapeutic effects of BNMNs on antioxidation and anti-inflammation

Given the significant antioxidant and anti-inflammatory effects of BNMNs in vivo, in vitro studies were conducted to investigate their underlying mechanisms. An in vitro release model was established by placing sterilized microneedle systems in fresh DMEM containing 100 μM H_2O_2 to simulate the oxidative stress microenvironment found in FNI and to release the encapsulated drugs. Based on the microneedle degradation rate in vivo and the drug release rate in vitro, the supernatant collected after 1 day of culture was selected for further analysis. The supernatant was then treated with 1.0 mM sodium pyruvate, 2.05 mM L-pyruvate, 10% fetal bovine serum, or 1% penicillin/streptomycin solution to neutralize H_2O_2 and maintain cell culture conditions. Prior to these experiments, the stability of 100 μM H_2O_2 under dark conditions at 37 °C was evaluated. After filtration through a 0.22 μm filter, the resulting solution was used as the corresponding group extract. The results showed that the 100 μM H_2O_2 solution remained highly stable over 5 days, with a concentration retention rate exceeding 90% (Figure S8A). Furthermore, the complete medium facilitated H_2O_2 degradation, reducing its concentration to below 1% within 20 min (Figure S8B).

RAW264.7 mouse macrophage cell line was derived from the BALB/c mouse leukemia virus-induced tumor because of its characteristics, including phagocytosis, cytokine secretion, and polarization potential, which are representative of monocyte/macrophage functions involved in inflammation [36]. Therefore, oxidative stress and inflammation were induced in macrophages using LPS, and they were treated with supernatants from different groups to evaluate the in vitro antioxidant and anti-inflammatory properties of various microneedle systems. The experimental groups were as follows: Control (G1), LPS (G2), LPS + MNs (G3), LPS+BMNs (G4), LPS+NMNs (G5), and LPS+BNMNs (G6) (Fig. 4A). The concentration of BPNs was measured in each group: the G6 group had a concentration of 60.2 ± 4.3 μg/mL, and the G4 group had 58.1 ± 3.1 μg/mL, with no significant statistical difference between the two groups (Figure S9). The DCF fluorescence assay was used to assess intracellular ROS levels.

BPN-containing microneedles rapidly neutralized intracellular ROS, confirming that nanosheet release translated into functional nanoredox activity in macrophages (Fig. 4B). Specifically, the G2 group exhibited significant green fluorescence compared to the G1 group, while the G4 and G6 groups showed almost no green fluorescence compared to the G2 group (Fig. 4C). Concurrently, the activities of catalase (CAT) and superoxide dismutase (SOD) were measured, revealing that CAT and SOD levels in the G4 and G6 groups were significantly higher than in the G2 group (Figure S10A and S10B). These results are consistent with previous studies showing that 5 μg/mL LPS effectively induces ROS production in macrophages, while BPNs possess exceptional antioxidant properties, enabling them to reduce ROS levels and mitigate oxidative stress [13, 37]. Further qRT-PCR analysis validated the significant anti-inflammatory effects of BNMNs. The G4 and G6 groups significantly inhibited the mRNA expression levels of pro-inflammatory cytokines, including *Tnf*, *Il6*, *Il1b*, and *Nos2*, while significantly promoting the mRNA expression levels of anti-inflammatory cytokines, including IL-10 and *Arg1* (Fig. 4D and I). Meanwhile, TNF-α and IL-1β are two key inflammatory factors that play essential roles in both acute and chronic inflammatory responses [38]. The protein levels of TNF-α and IL-1β were significantly reduced in the G4 and G6 groups (Fig. 4J and K). These results demonstrate that BPNs in the outer layer of microneedles exhibit outstanding antioxidant and anti-inflammatory efficacy. Notably, the G4 and G6 groups showed statistically significant reductions in the levels of these inflammatory markers compared to the LPS-induced G2 group. To further evaluate the regulatory effect of BNMNs on macrophage polarization, flow cytometry analysis was conducted to measure the surface markers CD86 (M1 macrophage marker) and CD206 (M2 macrophage marker) (Fig. 4L and M) [39]. Relative mean fluorescence intensity (MFI) quantification results for CD86 and CD206 indicate that, compared to the G2 group, the proportion of M1-type macrophages was significantly reduced in the G4 and G6 groups (Fig. 4N), while the proportion of M2-type macrophages was significantly increased (Fig. 4O). Finally, fluorescence microscopy

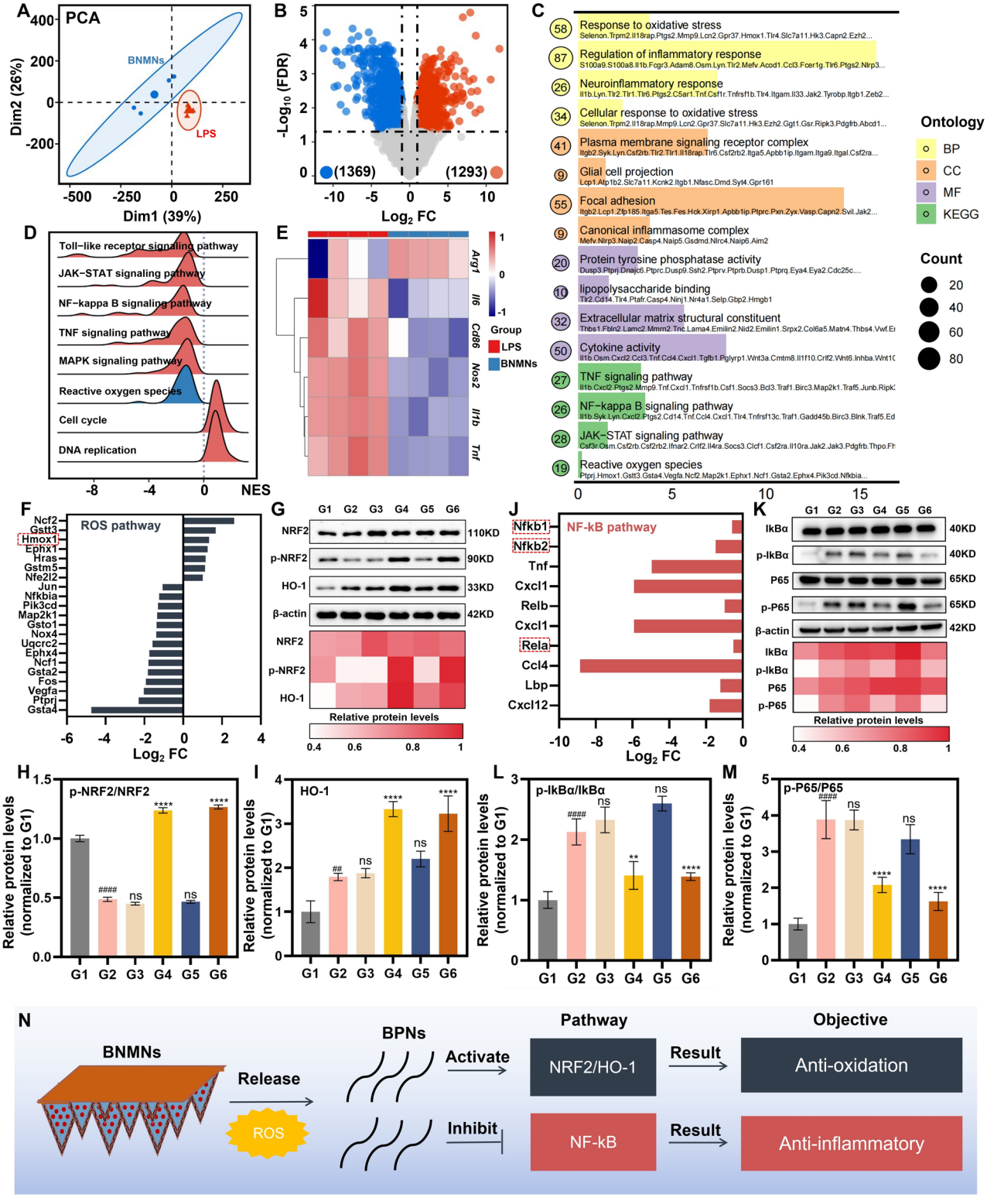

Fig. 5 (See legend on next page.)

(See figure on previous page.)

Fig. 5 Transcriptomic and mechanistic insights into BNMNs-mediated regulation of oxidative stress and inflammatory signaling pathways in LPS-stimulated macrophage. (**A**) Principal component analysis (PCA) showing distinct clustering of BNMNs-treated and LPS-treated groups. (**B**) Volcano plot showing significantly up- and down-regulated genes between the BNMNs and LPS groups. (**C**) Gene Ontology (GO) and Kyoto Encyclopedia of Genes and Genomes (KEGG) enrichment analyses highlighting biological processes (BP), Cellular Component (CC), Molecular Function (MF), and signaling pathways involved in oxidative stress and inflammatory response. **(D)** Gene set enrichment analysis (GSEA) identifying enriched signaling pathways. (**E**) Heatmap of representative inflammation- and oxidative stress-associated genes, including Il6, Nos2, Il1b, and Tnf across groups. (**F**) Differentially expressed genes in the ROS pathway. (**G**) Representative Western blot and semi-quantitative analysis of NRF2, phosphorylated NRF2 (p-NRF2), and HO-1 protein expression. (**H–I**) Quantification of p-NRF2/NRF2 and HO-1 expression levels normalized to β-actin. (**J**) NF-κB pathway-associated genes significantly altered by BNMNs treatment. (**K**) Western blot analysis of NF-κB signaling proteins, including IκBα, phosphorylated IκBα (p-IκBα), p65, and phosphorylated p65 (p-p65), with corresponding heatmap and quantification (**L–M**). (**N**) Schematic illustration of the proposed mechanism: ROS-responsive release of black phosphorus nanosheets (BPNs) from BNMNs activates the NRF2/HO-1 antioxidant pathway while concurrently suppressing the NF-κB inflammatory pathway, thereby exerting antioxidative and anti-inflammatory effects. Data are presented as mean ± SD ($n \geq 3$). Statistical significance: ns, not significant; $^{*}p < 0.05$, $^{**}p < 0.01$, $^{***}p < 0.001$ and $^{****}p < 0.0001$ compared with G2 group; $^{\#}p < 0.05$, $^{\#\#}p < 0.01$, $^{\#\#\#}p < 0.001$ and $^{\#\#\#\#}p < 0.0001$ compared with G1 group

images were consistent with flow cytometry analysis, both showing elevated Arg-1 protein expression in the G4 and G6 groups, along with a significant decrease in iNOS in these same groups (Fig. 4P and Q).

In summary, these findings highlight the robust antioxidant and anti-inflammatory properties of BNMNs in vitro, providing strong evidence for their potential therapeutic effects in alleviating oxidative stress and inflammation for FNI.

Mechanisms of BNMNs on antioxidation and anti-inflammation in vitro

Subsequently, the regulatory effects of BNMNs were investigated at the whole-transcriptome level by RNA-seq. Principal component analysis (PCA) revealed distinct clustering between the LPS and LPS + BNMNs groups, indicating marked transcriptomic differences between the two groups (Fig. 5A). The volcano plot further identified substantial changes in differentially expressed genes (DEGs), with 1,293 genes upregulated and 1,369 genes downregulated after BNMNs treatment (Fig. 5B). Kyoto Encyclopedia of Genes and Genomes (KEGG) enrichment analysis showed that these DEGs were mainly associated with inflammation- and oxidative stress-related pathways, including TNF, NF-κB, JAK/STAT, and ROS-related signaling pathways. Gene Ontology (GO) analysis further indicated that the enriched biological processes were closely related to oxidative stress and inflammatory regulation, including response to oxidative stress, regulation of inflammatory response, and cellular response to oxidative stress (Fig. 5C). Gene Set Enrichment Analysis (GSEA) revealed that, compared with the LPS group, the BNMNs group exhibited significant downregulation of key inflammation-associated signaling pathways, including Toll-like receptor, JAK-STAT, and NF-κB signaling pathways (Fig. 5D). Consistently, heatmap analysis showed that the anti-inflammatory and repair-associated gene Arg1 was generally upregulated, whereas pro-inflammatory genes, including Il6, Cd86, Nos2, Il1b, and Tnf, were generally downregulated in the BNMNs group (Fig. 5E). These results are consistent with our previous macrophage validation data and suggest that BPNs released early by BNMNs may modulate multiple inflammation- and oxidative stress-associated signaling pathways, thereby contributing to anti-inflammatory and antioxidant effects.

In addition, analysis of ROS-related DEGs showed that Hmox1, which encodes HO-1, was significantly upregulated after BNMNs treatment (Fig. 5F). To further explore the potential interaction between ROS regulation and NF-κB-mediated inflammatory signaling, a protein–protein interaction (PPI) network was constructed using representative DEGs associated with oxidative stress regulation and inflammatory responses. The PPI network revealed close functional interactions among redox- and inflammation-related molecules, including Nfe2l2, Hmox1, Nfkb1, Rela, Tnf, Il1b, Il6, and Nos2 (Figure S11). These transcriptomic and network-level findings suggest a coordinated immunoredox regulatory module in which BNMNs treatment is associated with activation of the NRF2/HO-1 antioxidant axis and suppression of NF-κB-related inflammatory signaling. Together with subsequent protein-level validation, these results support the involvement of NRF2/HO-1 and NF-κB signaling in BNMNs-mediated macrophage immunoredox remodeling.

To validate these transcriptomic findings, the NRF2/HO-1 pathway was studied by western blot (Fig. 5G), a critical regulator of cellular antioxidant defense [40]. The expression of p-NRF2/NRF2 was significantly upregulated in the G4 and G6 groups compared to the G2 group (Fig. 5H). This increase in p-NRF2 levels suggests that BNMNs promote NRF2 activation, thereby enhancing cellular defense mechanisms against oxidative stress. Additionally, HO-1 expression (Fig. 5I), a downstream target of NRF2, was also significantly elevated in the G4 and G6 groups, further confirming the activation of the NRF2/HO-1 pathway by BNMNs. Additionally, DEGs were enriched in the NF-κB signaling pathway, a key regulator of immune responses and inflammation [41], as shown in Fig. 5J. Western blot analysis further confirmed the involvement of the NF-κB signaling pathway in the anti-inflammatory effects of BNMNs (Fig. 5K). BNMNs treatment resulted in a significant decrease in the levels

of phosphorylated IκBα (p-IκBα), a critical inhibitor of NF-κB activation, as well as a reduction in the phosphorylation of p65, a key NF-κB subunit involved in the transcriptional regulation of pro-inflammatory cytokines (Fig. 5L and M). These findings support the hypothesis that BNMNs exert their anti-inflammatory effects by inhibiting the NF-κB pathway, thereby reducing the production of pro-inflammatory cytokines. The schematic representation in Fig. 5N summarizes the molecular mechanisms underlying the therapeutic effects of BNMNs. Upon ROS exposure, BNMNs released BPNs and shifted signaling toward an antioxidant state (NRF2/HO-1 activation) while dampening inflammatory signaling (NF-κB inhibition), aligning with the observed reductions in oxidative and pro-inflammatory readouts. This coordinated immunoredox modulation provides a mechanistic basis for using BNMNs as an early-phase intervention to mitigate the hostile injury microenvironment that limits peripheral nerve regeneration.

Ability of BNMNs to stimulate neural differentiation in vitro

In addition to their strong antioxidant and anti-inflammatory effects, BNMNs have demonstrated significant potential in promoting neuronal differentiation. To further investigate the therapeutic effects of BNMNs on neural injury and repair, an in vitro release model was utilized. After 5 days of treatment, the supernatant was treated with 1.0 mM sodium pyruvate, 2.05 mM L-pyruvate, 10% fetal bovine serum, or a 1% penicillin/streptomycin solution to neutralize H_2O_2 and maintain cell culture conditions. It was then collected and used for co-culture with PC12 or RSC96 cells. The experimental groups were as follows: Control (G1), H_2O_2-induced blank control (G2), H_2O_2-induced MNs (G3), H_2O_2-induced BMNs (G4), H_2O_2-induced NMNs (G5), and H_2O_2-induced BNMNs (G6) (Fig. 6A). The G2 group represented the same H_2O_2 supernatant, but after the addition of complete medium, which neutralizes or clears the H_2O_2 to simulate the cellular environment after oxidative stress is removed. Meanwhile, NGF concentration was measured in each group: the G6 group had 29.2 ± 1.2 ng/mL, and the G5 group had 30.3 ± 2.3 ng/mL, with no significant difference between the two groups (Figure S12). The PC12 cell line, derived from rat pheochromocytoma cells, is a classical model for studying neuronal differentiation due to its ability to extend neurites and differentiate upon NGF stimulation [42]. Subsequently, phalloidin staining was used to visualize PC12 cell morphology and assess the effects of different treatments on neurite outgrowth. The G6 group exhibited significantly more robust, elongated neurites tqueryan all other experimental groups, highlighting the synergistic effect of sequential BPN/NGF delivery (Fig. 6B). Quantitative analysis of cell numbers (Fig. 6C) and neurite lengths (Fig. 6D) further confirmed these observations.

Next, the expression of key neurogenic markers was assessed, including *Tuj1*, *Gap43*, and *Map2*, which are essential for neuronal differentiation and axonal growth [43, 44]. The mRNA expression of key neurogenic markers, including *Tuj1*, *Gap43*, and *Map2*, was significantly upregulated in the G6 group compared to the other treatment groups. Specifically, the G6 group exhibited markedly higher levels of *Tuj1* (Fig. 6E), *Gap43* (Fig. 6F), and *Map2* (Fig. 6G), suggesting that BNMNs promote neuronal differentiation and maturation. This upregulation of neurogenic markers is consistent with the observed enhancement of neurite outgrowth in the BNMNs-treated group, indicating their potential to facilitate neuronal growth and development.

In addition to promoting neurite outgrowth and neuronal differentiation, BNMNs activate key neurotrophic signaling pathways, crucial for neuronal survival and differentiation. TrkA, a receptor tyrosine kinase, plays a pivotal role in the NGF-mediated signaling cascade. Upon binding to NGF, TrkA undergoes autophosphorylation, triggering the activation of downstream pathways critical for neuronal survival and differentiation [45]. To investigate this further, western blot analysis was conducted to measure the levels of total and phosphorylated forms of proteins involved in neurotrophic signaling, including TrkA, AKT, and CREB (Fig. 6H). The results revealed significant differences in the activation of these pathways among the treatment groups. TrkA phosphorylation (p-TrkA) was notably higher in the G6 group, compared to the other groups (Fig. 6I). Since TrkA activation is a critical mechanism in NGF-mediated neurotrophic signaling, these results suggest that BNMNs enhance neuronal differentiation via TrkA-dependent signaling. Moreover, activation of downstream signaling molecules, such as AKT and CREB, was significantly higher in the G6 group than in the other groups. The AKT pathway, activated by TrkA, is well known for promoting cell survival, growth, and differentiation [8]. Phosphorylated AKT (p-AKT), found at higher levels in G5 and G6 groups (Fig. 6J), supports neuronal survival and plays a key role in enhancing neuronal growth. The CREB pathway, another key neurotrophic signaling pathway, was also significantly activated in the G6 group (Fig. 6K). CREB phosphorylation (p-CREB) promotes neuroprotection, neurogenesis, and synaptic plasticity [46], further supporting the role of BNMNs in promoting neuronal differentiation and maturation. Additionally, the stress-activated protein kinases, including JNK, ERK, and p38, are activated by stress signals and play important roles in neuronal differentiation and survival [47, 48]. In our study, phosphorylation of JNK, ERK, and p38 was increased in the G6 group (Fig. 6L and O). Among these

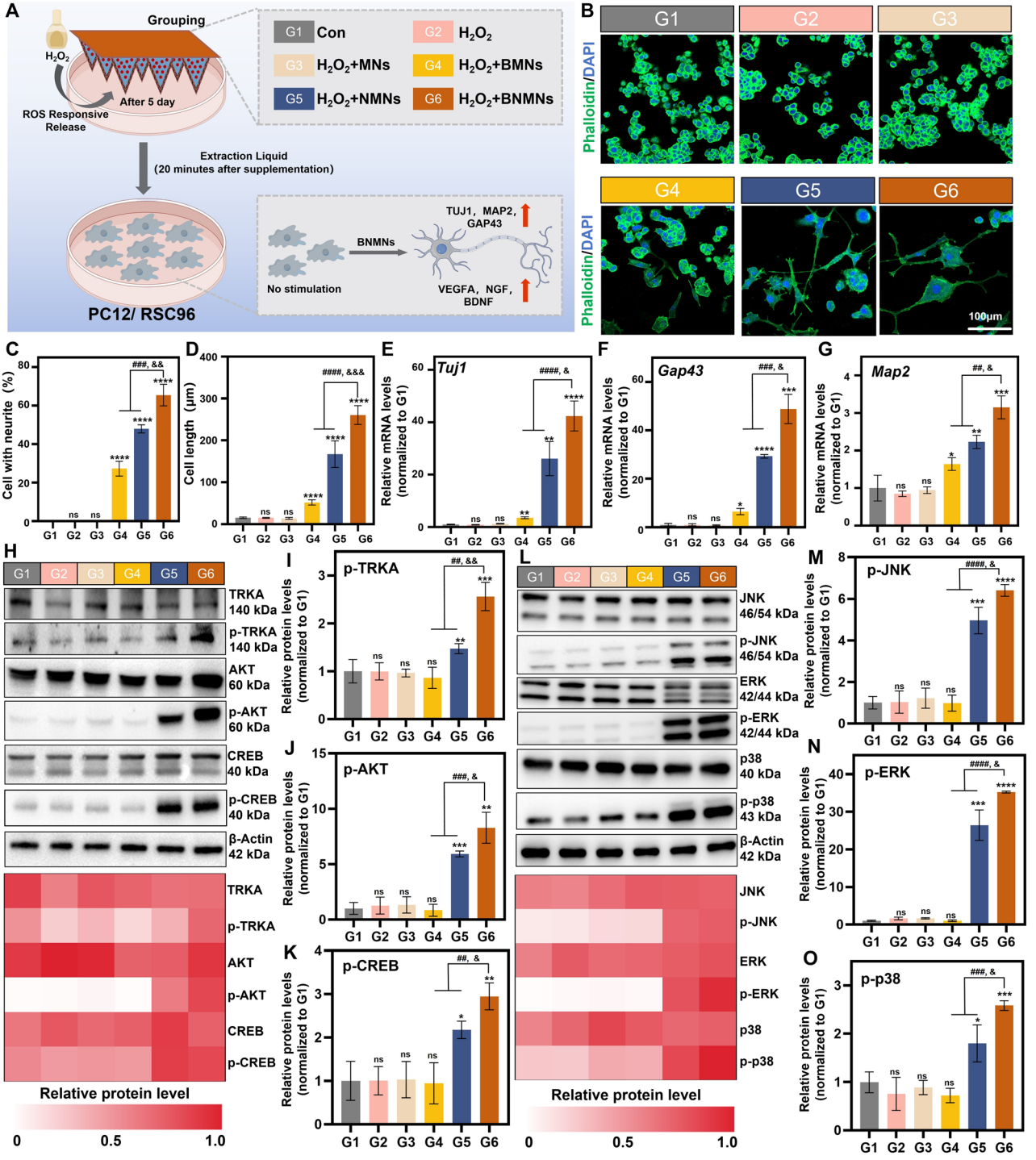

Fig. 6 Effects of ROS-Responsive BNMNs on PC12 cell differentiation and TrkA signaling pathway. (**A**) Schematic illustration of the experimental design showing the effects of different ROS-responsive microneedle systems on PC12 and RSC96 cells after 5 days of release. The experiment was divided into six groups: Control (G1), H_2O_2 (G2), H_2O_2 + MNs (G3), H_2O_2 + BMNs (G4), H_2O_2 + NMNs (G5), and H_2O_2 + BNMNs (G6). (**B**) Representative images showing the morphology of PC12 cells across groups, with Phalloidin staining for the cytoskeleton (green) and DAPI staining for the nucleus (blue). (**C**) Quantification of the number of cells with neurites in each group. (**D**) Quantification of cell length in each group. Relative mRNA expression levels of (**E**) *Tuj1*, (**F**) *Gap43*, and (**G**) *Map2*. (**H**) Western blot analysis showing protein expression of TrkA, p-TrkA, p-AKT, AKT, p-CREB, and CREB. Statistical analysis of relative protein levels of (**I**) p-TRKA, (**J**) p-AKT, (**K**) p-CREB. (**L**) Western blot analysis showing protein expression of JNK, p-JNK, ERK, p-ERK, p38, and p-p38. Statistical analysis of relative protein levels of (**M**) p-JNK, (**N**) p-ERK, and (**O**) p-p38. Data are presented as mean ± SD ($n = 3$). Statistical significance: ns, not significant; $^{*}p < 0.05$, $^{**}p < 0.01$, $^{***}p < 0.001$ and $^{****}p < 0.0001$ compared with G1 group; $^{\#\#}p < 0.01$, $^{\#\#\#}p < 0.001$ and $^{\#\#\#\#}p < 0.0001$ compared with G4 group; $^{\&}p < 0.05$, $^{\&\&}p < 0.01$ and $^{\&\&\&}p < 0.001$ compared with G5 group

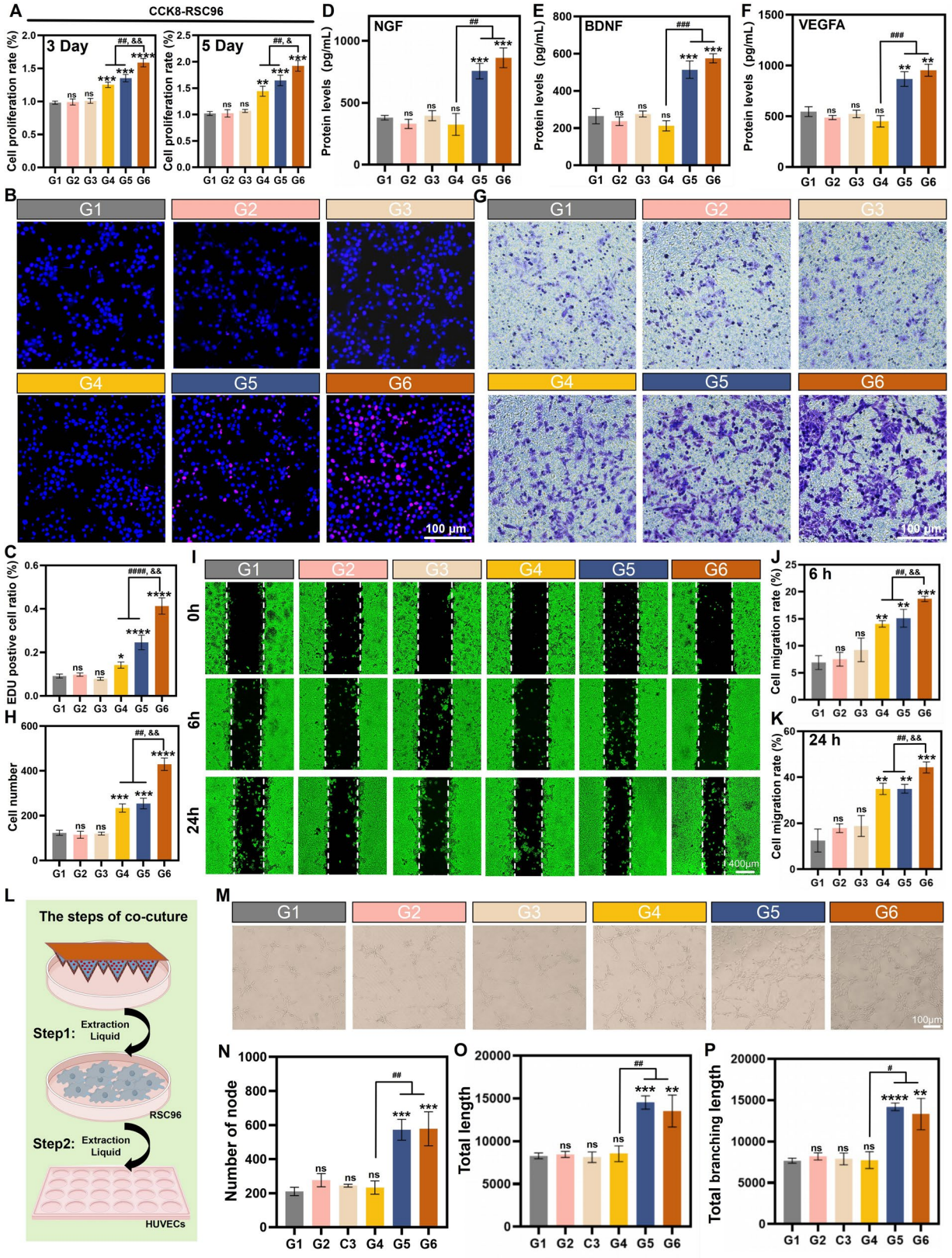

Fig. 7 (See legend on next page.)

(See figure on previous page.)

Fig. 7 Effects of ROS-Responsive BNMNs on RSC96 cell proliferation, migration, and angiogenic factors. (**A**) CCK-8 assay showing the cell proliferation rate of RSC96 cells at 3 days and 5 days post-treatment. (**B**) Representative EdU staining images showing proliferating cells (blue: nuclei, green: EdU) across groups. (**C**) Quantification of EdU-positive cell ratio at 24 h. Quantification of protein levels of (**D**) NGF, (**E**) BDNF, and (**F**) VEGFA in RSC96 cell culture supernatants after treatment with different microneedle systems. (**G**) Representative crystal violet staining images of RSC96 cells to assess cell migration across groups. (**H**) Quantification of the total number of cells in each group. **(I)** Representative images from the wound healing assay at 0 h, 6 h, and 24 h post-treatment. Cell migration assay at (**J**) 6 h and (**K**) 24 h showing the relative migration rate across the different groups. **(L)** Schematic diagram of the co-culture experimental design, where RSC96 cells and HUVECs were co-cultured using the extract from different microneedle systems. (**M**) Representative images of tube-like structure formation in each group after treatment. (**N-P**) Angiogenesis assay showing the (**N)** number of nodes, (**O**) total length, and (**P**) total branching length in the co-culture system. Data are presented as mean ± SD ($n = 3$). Statistical significance: ns, not significant; $^{*}p < 0.05$, $^{**}p < 0.01$, $^{***}p < 0.001$ and $^{****}p < 0.0001$ compared with G1 group; $^{\#}p < 0.05$, $^{\#\#}p < 0.01$ and $^{\#\#\#}p < 0.001$ compared with G4 group; $^{\&}p < 0.05$ and $^{\&\&}p < 0.01$ compared with G5 group

MAPK pathways, ERK activation is a well-established downstream event of NGF/TrkA signaling in PC12 cells and is closely associated with neurite outgrowth, neuronal differentiation, and survival. The enhanced ERK phosphorylation observed in the G6 group, therefore, supports the activation of NGF-mediated neurotrophic signaling by BNMNs. In contrast, JNK and p38 are stress-responsive MAPK pathways with context-dependent functions. In our system, the combined BPNs/NGF-containing microenvironment provided by BNMNs may modulate MAPK signaling dynamics, leading to balanced activation of JNK and p38, which may be associated with adaptive cellular responses rather than cytotoxic stress. Together, these findings suggest that BNMNs may promote neuronal maturation and survival by enhancing NGF/TrkA–ERK signaling while modulating broader MAPK stress-response pathways.

Taken together, the activation of the TrkA, AKT, CREB, and ERK pathways by BNMNs not only promotes neuronal differentiation but also enhances neuronal survival and maturation. These findings highlight the key role of TrkA signaling in mediating the effects of BNMNs, suggesting that the BNMN-induced activation of these pathways is essential for supporting neuronal development and neuroprotection.

Ability of BNMNs to stimulate schwann cell (SC) repair in vitro

The proliferation and migration of RSC96 cells (hereafter referred to as Schwann cells, SCs) in response to treatment with various microneedle systems were investigated. A rat Schwann cell line, RSC96, derived from peripheral nerve tissue and characterized by its glial-like functions, including the secretion of neurotrophic factors and support for axonal regeneration, was used to mimic Schwann cell–associated microenvironments [49]. The cytotoxicity of different groups was assessed on day 5 of SC culture, with results indicating favorable safety profiles across all groups (Figure S13A and S13B). The CCK-8 assay revealed that the G4, G5, and G6 groups significantly increased SC proliferation compared to the G1 group on both days 3 and 5, with the G6 group exhibiting the highest proliferation rate (Fig. 7A).

To further investigate cell proliferation at 24 h, an EdU incorporation assay was performed, which showed a higher percentage of EdU-positive cells in the G6 group compared to the G1, G4, and G5 groups, indicating increased DNA synthesis and cell proliferation (Fig. 7B and C). This suggests that BNMNs promote cell proliferation, potentially contributing to tissue regeneration processes. Further, protein levels of neurotrophic factors crucial for neurorepair and regeneration were assessed, including NGF (Fig. 7D), BDNF (Fig. 7E), and VEGFA (Fig. 7F). The results revealed that the G5 and G6 groups significantly upregulated these factors compared to the G1 group. These findings suggest that BNMNs not only support cell proliferation but also enhance the secretion of key neurotrophic factors involved in neurogenesis and tissue repair. To assess the effects of BNMNs on SC migration, both Transwell and scratch wound healing assays were performed. The Transwell results showed that the G6 group had a higher migratory capacity than the G1, G4, and G5 groups (Fig. 7G and H). Meanwhile, scratch wound healing assays at 6 h and 24 h showed that cell migration was significantly higher in the G6 group at both time points compared with the G1, G4, and G5 groups (Fig. 7I and K). These findings confirm that BNMNs not only promote cell proliferation but also enhance SC migratory capacity, which is essential for tissue regeneration. Finally, the potential of BNMNs to influence endothelial cell behavior was explored using a co-culture system with HUVECs (Fig. 7L). The G4 and G6 treatments significantly promoted endothelial cell function, including node formation (Fig. 7N), total length (Fig. 7O), and branching length (Fig. 7P), compared with the other groups. These findings suggest that BNMNs facilitate endothelial cell network formation, which is essential for angiogenesis and tissue repair.

Taken together, these results highlight that BNMNs not only stimulate SC proliferation and migration but also enhance the secretion of neurotrophic factors and endothelial cell function, underscoring their potential to promote tissue regeneration and repair following nerve injury.

Conclusion

In summary, we developed a ROS-adaptive core–shell microneedle platform that couples early immunoredox remodeling with sustained neurotrophic stimulation for facial nerve repair. By leveraging dynamic covalent chemistry, we engineered a shell composed of a hyaluronic acid–phenylboronic acid/poly(vinyl alcohol) (HA–PBA/PVA) network, enabling ROS-responsive shell disassembly and early release of black phosphorus nanosheets (BPNs). This early intervention attenuated pathological ROS accumulation, supported NRF2/HO-1-associated antioxidant responses, and reduced NF-κB-related inflammatory activation, thereby promoting a more permissive immune microenvironment. The GelMA hydrogel core served as a local reservoir for nerve growth factor (NGF), allowing sustained NGF release and subsequent neurotrophic stimulation. In a mouse facial nerve crush model, BNMNs treatment improved early functional recovery, enhanced myelin structural repair, and showed favorable short-term biosafety. Compared with blank or single-cargo microneedle treatments, BNMNs were associated with stronger activation of TrkA/AKT/ERK signaling and improved regenerative outcomes. Overall, this work provides a temporally programmed microneedle-based strategy for addressing stage-dependent barriers in peripheral nerve repair and offers a potentially adaptable platform for ROS-associated tissue injuries.

Despite these promising results, several considerations remain for clinical translation and mechanistic refinement. First, the 14-day in vivo endpoint used in this study is sufficient to capture early-stage oxidative stress resolution, inflammatory remodeling, initial remyelination, and early functional recovery; however, it is relatively short for evaluating complete peripheral nerve regeneration. Therefore, the current findings should be interpreted as evidence of accelerated early repair rather than definitive proof of full long-term regeneration. Future long-term studies extending to 28–42 days will be necessary to assess late-stage axonal maturation, myelin sheath stabilization, G-ratio normalization, nerve conduction recovery, and the durability of functional improvement. In addition, these longer-term experiments should evaluate whether BNMNs treatment prevents denervation-induced target muscle atrophy, preserves neuromuscular junction integrity, and improves long-term facial muscle function. Second, while our study demonstrates short-term efficacy in a mouse facial nerve crush model, long-term stability and sustained functional outcomes should be further validated in larger animal models to bridge the gap between rodent physiology and human pathology. Furthermore, although we focused primarily on macrophage polarization, the broader in vivo crosstalk among neutrophils, T cells, Schwann cells, fibroblasts, and vascular cells during long-term remodeling remains to be fully mapped. Importantly, the macrophage polarization results in this study were primarily derived from the RAW264.7 cell line, which may not fully recapitulate the behavior of primary macrophages. Therefore, future studies should validate these findings using primary macrophages, such as bone marrow-derived macrophages or peritoneal macrophages, to strengthen the physiological and translational relevance of the observed anti-inflammatory effects. Further optimization of microneedle geometry will be important for improving delivery efficiency across different injury locations, while long-term studies are needed to assess the safety profile of prolonged material degradation. Ultimately, the modular nature of this core–shell design provides a robust chemical engineering framework for developing intelligent biomaterials capable of orchestrating complex tissue regeneration through programmed, multi-stage therapeutic interventions.

Supplementary Information

The online version contains supplementary material available at https://doi.org/10.1186/s12951-026-04647-0.

Supplementary Material 1.

Supplementary Material 2.

Author contributions

Qiang Zhou, Qingyue Yuan, Peng Lai, and Shuo Li contributed to the study design and to the writing and editing of the paper. Xianlong Wang, Yuqi Han, Shuyi Lin, Chenhao Fang, Kaizheng Qu, Ziwei Zhang, and Ying Ran conducted the study and analyzed the data. Yiheng Yang, Yavuz Nuri Ertas, Liangle Liu, and Xianzhen Chen supervised the research, revised the paper, and secured funding for the project. All the authors reviewed the manuscript.

Funding

The authors acknowledge financial support from the National Natural Science Foundation of China (82571581).

Data availability

Data will be available on request.

Declarations

Competing interests

The authors declare no competing interests.

Author details

[1]Department of Neurosurgery, Shanghai Tenth People's Hospital, School of Medicine, Tongji University, Shanghai 200072, China
[2]Department of Neurosurgery, Shanghai Tenth People's Hospital, Clinical Medical College of Nanjing Medical University, Nanjing 211166, China
[3]Department of Orthopedics, Shanghai General Hospital, Shanghai Jiao Tong University School of Medicine, Shanghai 200080, China
[4]Shanghai Tenth People's Hospital, School of Medicine, Clinical Medicine Scientific and Technical Innovation Center, Tongji University, Shanghai 200072, China
[5]Department of Dermatology, Shanghai Skin Disease Hospital, Tongji University School of Medicine, Shanghai 200443, China
[6]Xiangnan Hospital Affiliated to Hunan Normal University/922nd Hospital of Joint Logistics Support Force, PLA, Hengyang 421000, China
[7]Department of Biomedical Engineering, Erciyes University, Kayseri 38039, Türkiye

[8]Mini-invasive Interventional Therapy Center, Shanghai East Hospital, Tongji University, Shanghai 200120, China
[9]Department of Spine Surgery, The Third Affiliated Hospital of Wenzhou Medical University, Wenzhou 325200, China

Received: 12 March 2026 / Accepted: 27 May 2026
Published online: 08 June 2026

References

1. Lin L, Yuan X, Ma L, Xu L, Xie W, Jiang Y, Xiu J, Xu H, Tian Z, Qu J, Zhao C, Yuan Z, Liu H, Huang J, Wang X. Bioact Mater. 2025;53:630.
2. Ma J, Yan J, Su N, Qiu Z, Hou H, Sun J, Sun X, Niu Y, He L. J Mol Histol. 2025;56:67.
3. Xue R, Xie M, Wu Z, Wang S, Zhang Y, Han Z, Li C, Tang Q, Wang L, Li D, Wang S, Yang H, Zhao RC. Aging dis. 2024;15:851.
4. Lee J, Yeo JH, Kim SS, Lee JM, Yeo SG. Antioxidants. 2025;14:436.
5. Colak B, Cihan MC, Ertas YN. ACS Appl Nano Mater. 2023;6:16076.
6. Yasui G, Yamamoto Y, Shichinohe R, Funayama E, Oyama A, Hayashi T, Furukawa H. J Plast Reconstr Aesthet Surg. 2016;69:328.
7. Hai Q, Wang Y, Li H, Pei H, Wang N, Zhang X, Fan M, Liao J, Wen W, Zhao J, Yang L, Cui H. J Cell Mol Med. 2025;29:e70571.
8. Wuhanqimuge A, Itakura Y, Matsuki M, Tanaka M, Arioka. FEBS Open Bio. 2013;3:243.
9. Kropf E, Fahnestock M. *Cells* 2021, *10*, 1983.
10. Clewes O, Fahey MS, Tyler SJ, Watson JJ, Seok H, Catania C, Cho K, Dawbarn D, Allen SJ. J Neurochem. 2008;107:1124.
11. Bruno MA, Leon WC, Fragoso G, Mushynski WE, Almazan G, Cuello AC. J Neuropathol Exp Neurol. 2009;68:857.
12. Chen L, Shi L, Wei T, Liu H, Wang Z, Wang H, Li N, Feng S. Acta Biomater. 2025;202:529.
13. He M, Zhang X, Ran X, Zhang Y, Nie X, Xiao B, Lei L, Zhai S, Zhu J, Zhang J, Li R, Liu Z, Zhu Y, Dai Z, He Z, Feng J, Zhang C. Adv Mater. 2024;36:2404576.
14. Shen J, Jia G, Wu Q, Yang H, Jiang Y, Wu X, Chai Y, Zhang C, Xu J. J Controlled Release. 2025;380:579.
15. He Z, Chen W, Hu K, Luo Y, Zeng W, He X, Li T, Ouyang J, Li Y, Xie L, Zhang Y, Xu Q, Yang S, Guo M, Zou W, Li Y, Huang L, Chen L, Zhang X, Saiding Q, Wang R, Zhang M-R, Kong N, Xie T, Song X, Tao W. Nat Nanotechnol. 2024;19:1386.
16. Ran Y, Shi J, Ding Y, Li L, Lu D, Zeng Y, Qiu D, Yu J, Cai X, Pan Y. Adv Sci. 2024;11:2409155.
17. Su H, Ye Q, Wang D, Liu A, Wang Y, Zhang Y, Weng L. Biofabrication. 2025;17:025031.
18. Ertas YN, Ertas D, Erdem A, Segujja F, Dulchavsky S, Ashammakhi N. *Small* 2024, *20*, 2308479.
19. Choi HJ, Ullah A, Jang MJ, Lee US, Shin MC, An SH, Kim D, Kim BH, Kim GM. Sci Rep. 2024;14:19228.
20. Ullah A, Khan H, Choi HJ, Kim GM. Polymers. 2019;11:1834.
21. Yilmaz H, Karzoun L, Ozturk Guzelcan Bl, Sahin H, Kazancioglu Y, Habra MY, Yuca Yilmaz E, Guzel E, Gunduz O, Ertas YN, Ustundag CB. ACS Appl Bio Mater. 2026;9:1888.
22. Pan W, Dai C, Li Y, Yin Y, Gong L, Machuki JO, Yang Y, Qiu S, Guo K, Gao F. Biomaterials. 2020;239:119851.
23. L QBWJQ, A M, Y L, B G. *Regenerative Biomaterials* 2023, *11*.
24. Wang Y, Liu Q, Xu Y, Zhang Y, Lv Y, Tan Y, Jiang N, Cao G, Ma X, Wang J, Cao Z, Yu B, Kou J. Int J Biol Sci. 2016;12:1341.
25. Negro S, Lauria F, Stazi M, Tebaldi T, D'Este G, Pirazzini M, Megighian A, Lessi F, Mazzanti CM, Sales G, Romualdi C, Fillo S, Lista F, Sleigh JN, Tosolini AP, Schiavo G, Viero G, Rigoni M. Acta Neuropathol Commun. 2022;10:189.
26. Zhou Q, Shubhra QTH, Lai P, Shi J, Fang C, Guo Q, Li W, Chen R, Shen X, Huang L, Cai X, Lin S. Adv Compos Hybrid Mater. 2025;8:145.
27. Sert NPD, Hurst V, Ahluwalia A, Alam S, Avey MT, Baker M, Browne WJ, Clark A, Cuthill IC, Dirnagl U, Emerson M, Garner P, Holgate ST, Howells DW, Karp NA, Lazic SE, Lidster K, MacCallum CJ, Macleod M, Pearl EJ, Petersen OH, Rawle F, Reynolds P, Rooney K, Sena ES, Silberberg SD, Steckler T, Würbel H. PLOS Biol. 2020;18:e3000410.
28. Unit of Biostatistics and Research Methodology, School of Medical Sciences, Universiti Sains Malaysia, 16150 Kubang Kerian, Kelantan, Malaysia, W. M. Z. Wan Mohammad, Department of Community Medicine, School of Medical Sciences, Universiti Sains Malaysia, 16150 Kubang Kerian, Kelantan, Malaysia, Malays. J. Med. Sci. 2017, *24*, 101.
29. Most SP. Arch Facial Plast Surg. 2004;6:82.
30. Hui L, Yuan J, Ren Z, Jiang X. Neurosci (Riyadh Saudi Arab). 2015;20:65.
31. Wu Z, Cheng W, Su J. Eur Cell Mater. 2025;53:52.
32. Karlsson M, Kurz T, Brunk UT, Nilsson SE, Frennesson CI. Biochem J. 2010;428:183.
33. Oshima E, Hayashi Y, Xie Z, Sato H, Hitomi S, Shibuta I, Urata K, Ni J, Iwata K, Shirota T, Shinoda M. J Neuroinflamm. 2023;20:258.
34. Lu X, Xu R, Dong X, Bai D, Ji W, Chen X, Chen H, Hou C, Gao J. Stem Cell Res Ther. 2025;16:297.
35. Guo P, Huang C, Yang Q, Zhong G, Zhang J, Qiu M, Zeng R, Gou K, Zhang C, Qu Y. Int J Nanomed. 2023;18:7759.
36. Lu H, Zhou Q, Li J, Xu S, Yu L, Zhu Y, Zhang H, Shi C, Zuo T, Xu M, Su M, Zhang Y, Hu R, Shubhra QTH, Deng H, Hu X, Cai X. Adv Sci. 2025;12:2500116.
37. Liu Z, Shen Z, Lu H, Lu B, Zhang P, Chen W, Huang G, Qu X, Yu Z, Chen F, Zang W. ACS Nano. 2026;20:1431.
38. Dos Santos MG, Arbo BD, Hort MA. Neural Regen Res. 2026;21:1783.
39. Liu L, Stokes JV, Tan W, Pruett SB. J Immunol Methods. 2022;511:113378.
40. Chen H, Xie K, Chen Y, Wang Y, Wang Y, Lian N, Zhang K, Yu Y. Int Immunopharmacol. 2019;75:105746.
41. Sun S-C. Nat Rev Immunol. 2017;17:545.
42. Wiatrak B, Kubis-Kubiak A, Piwowar A, Barg E. Cells. 2020;9:958.
43. Su W-T, Shih Y-A. Biomed Mater Eng. 2015;26:S189.
44. Hua P, Pan X, Liu J, Chen X, Li M, Guo Y, Li X, Leng P, Fan G, Zheng M, Yu K, Ma P, Zhang C, Shen X. Chem Eng J. 2025;514:163246.
45. Fukaya M, Ibuchi K, Sugawara T, Itakura M, Ito A, Shiroshima T, Hara Y, Okamoto H, Luton F, Sakagami H. Traffic. 2024;25:e12936.
46. Ospondpant D, Gao X, Lin S, Ho YM, Dong TTX, Tsim KWK. J Agric Food Chem. 2025;73:9595.
47. Pan B, Sun J, Liu Z, Wang L, Huo H, Zhao Y, Tu P, Xiao W, Zheng J, Li J. J Adv Res. 2021;33:215.
48. Liu J, Lu Y, Tang M, Shao F, Yang D, Chen S, Xu Z, Zhai L, Chen J, Li Q, Wu W, Chen H. Mar Drugs. 2022;20:245.
49. Ji Y, Shen M, Wang X, Zhang S, Yu S, Chen G, Gu X, Ding F. J Proteome Res. 2012;11:3186.

Publisher's note